JBC RESEARCH ARTICLE

TatA and TatB generate a hydrophobic mismatch important for the function and assembly of the Tat translocon in *Escherichia coli*

Received for publication, December 10, 2021, and in revised form, June 21, 2022 Published, Papers in Press, July 7, 2022,
https://doi.org/10.1016/j.jbc.2022.102236

Denise Mehner-Breitfeld[1], Michael T. Ringel[1], Daniel Alexander Tichy[1,2], Laura J. Endter[2], Kai Steffen Stroh[2], Heinrich Lünsdorf[3], Herre Jelger Risselada[2], and Thomas Brüser[1,*]

From the [1]Institute of Microbiology, Leibniz Universität Hannover, Hannover, Germany; [2]Institute for Theoretical Physics, Georg August University Göttingen, Göttingen, Germany; [3]Electron Microscopy Unit, Helmholtz Centre of Infection Research, Braunschweig, Germany

Edited by Chris Whitfield

The twin-arginine translocation (Tat) system serves to translocate folded proteins across energy-transducing membranes in bacteria, archaea, plastids, and some mitochondria. In *Escherichia coli*, TatA, TatB, and TatC constitute functional translocons. TatA and TatB both possess an N-terminal transmembrane helix (TMH) followed by an amphipathic helix. The TMHs of TatA and TatB generate a hydrophobic mismatch with the membrane, as the helices comprise only 12 consecutive hydrophobic residues; however, the purpose of this mismatch is unclear. Here, we shortened or extended this stretch of hydrophobic residues in either TatA, TatB, or both and analyzed effects on translocon function and assembly. We found the WT length helices functioned best, but some variation was clearly tolerated. Defects in function were exacerbated by simultaneous mutations in TatA and TatB, indicating partial compensation of mutations in each by the other. Furthermore, length variation in TatB destabilized TatBC-containing complexes, revealing that the 12-residue-length is important but not essential for this interaction and translocon assembly. To also address potential effects of helix length on TatA interactions, we characterized these interactions by molecular dynamics simulations, after having characterized the TatA assemblies by metal-tagging transmission electron microscopy. In these simulations, we found that interacting short TMHs of larger TatA assemblies were thinning the membrane and—together with laterally-aligned tilted amphipathic helices—generated a deep V-shaped membrane groove. We propose the 12 consecutive hydrophobic residues may thus serve to destabilize the membrane during Tat transport, and their conservation could represent a delicate compromise between functionality and minimization of proton leakage.

Tat systems serve the purpose to transport folded proteins across energy-transducing membranes in bacteria, archaea, plastids, and some mitochondria (1–3). They minimally consist of two components, TatA and TatC (4), but three-component TatABC systems are very common and found in the model Tat systems of *Escherichia coli* and plant plastids (5). TatA and TatB are structurally similar and evolutionary related (6). Both are membrane anchored by a 13 to 15 residues long N-terminal transmembrane helix (TMH) that contains only 12 consecutive hydrophobic residues. This helix is connected to an amphipathic helix (APH) *via* a short hinge at the cytoplasmic surface of the membrane (7–10) (Fig. 1*A*). The APH is followed by a negatively charged patch of residues in TatA (11), and more C-terminal regions are neither conserved nor functionally essential (12). TatC has six transmembrane domains with both termini on the cytoplasmic side (13, 14). TatB interacts tightly with TatC, whereas TatA gradually dissociates during purifications (15–17). From studies employing cross-linking and fluorescent protein tagging, it is known that the TatA interaction with TatBC changes during the translocation cycle, and larger TatA assemblies at TatABC complexes are believed to enable transport (18–23). A subpopulation of TatA protomers interacts with TatBC in a way that is not affected by mutations in TatC that abolish substrate binding (15), and resting-state-contacts of TatA to TatC have been identified (24). TatA assemblies undergo substrate-induced conformational changes that relate to Tat transport (25, 26), and the TatABC components rearrange during the translocation cycle (27, 28).

Tat-dependently transported proteins possess an N-terminal signal peptide that contains a highly conserved eponymous twin-arginine motif (1, 29). This motif is recognized by TatBC complexes that catalyze the membrane insertion of the signal peptide (30), whereas TatA is primarily required for the translocation step (18). TatA shows a high tendency to self-associate (31–34), but high-resolution structures are only available for detergent-solubilized TatA (7, 8, 10), and the mode of TatA self-interactions in membranes is still unclear. Spin-labeling studies indicated that the TMHs of TatA laterally interact (35), but only circular arrangements of aligned TatA have been suggested (8), and the orientation of the APH has not been included in the latest models (36). Interestingly, a dimeric structure of detergent-solubilized TatA indicated that also APHs of neighboring TatA protomers laterally interact (10).

* For correspondence: Thomas Brüser, brueser@ifmb.uni-hannover.de.

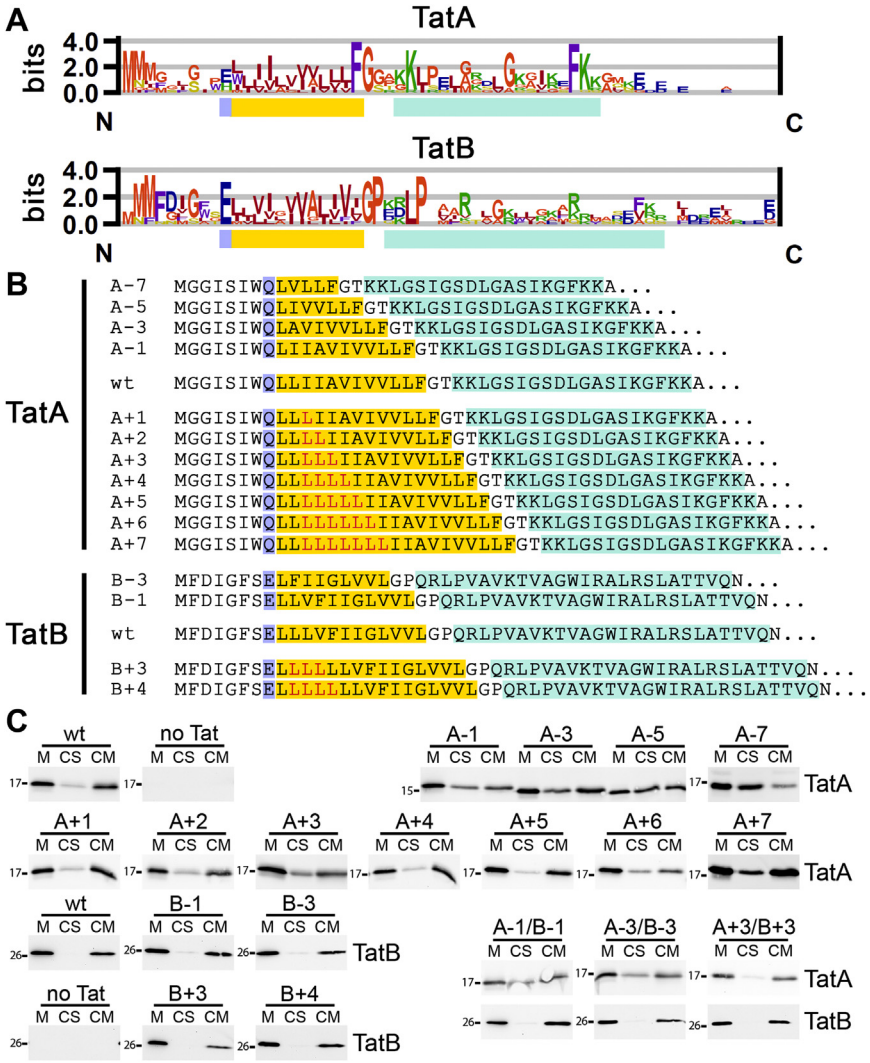

Figure 1. Constructs for the analysis of the 12-residues hydrophobic stretch in TatA and TatB. *A*, sequence logos of the functionally important region of TatA and TatB. Highlighted are the 12-residues hydrophobic stretch in the transmembrane helix of TatA and TatB (*yellow*), the preceding polar position (*bluish purple*), and the amphipathic helix (*turquoise*). The sequence logos have been obtained using enoLOGOS (88) based on sequence alignments by Clustal Omega (89) of sequences from a wide range of organisms, including α-, β-, γ-, δ-, and ε-proteobacteria, firmicutes, actinobacteria, cyanobacteria, chlorobi, chloroflexaceae, thermodesulfobacteria, aquificae, archaea, and plant plastids. *B*, TatA and TatB variants used in this study. The color code is the same as in (*A*). Inserted Leu residues are in *red*. *C*, carbonate wash analysis for the assessment of membrane integration of the TatA and TatB variants used in this study. TatA or TatB variants were detected by SDS-PAGE/Western blotting in the untreated membrane fraction (M), supernatant after carbonate wash (CS), and membranes after carbonate wash (CM). Molecular weight marker positions (kDa) are indicated. Note that all analyzed TatA and TatB variants are membrane inserted, but TatB variants are more stably membrane inserted than TatA variants, most likely due to their tighter interaction with TatC. The shorter the membrane anchor of TatA, the more was extracted by carbonate treatment.

TMHs need to span the ca. 3 nm thick hydrocarbon core of membranes, and about 20 hydrophobic residues could in principle do this, but TMHs are in average 24.0 ± 5.6 residues long (37), which is generally due to flexing or tilting of helices in membranes (38). It is therefore very unusual that TatA and TatB have membrane anchors with TMHs of 13 to 15 residues that contain only 12 consecutive hydrophobic residues, and that the length of this 12-residues stretch is strictly conserved from archaea to bacteria (Fig. 1*A*). As this short length does not suffice to span a membrane lipid bilayer of normal thickness, the TMHs of TatA and TatB generate a hydrophobic mismatch. It has been found that the TMH of TatA per se can destabilize membranes (25), but potential effects of helix shortenings or extensions have never been systematically analyzed.

We therefore changed the hydrophobic mismatch of TatA and TatB by generating helix shortenings and extensions and investigated effects on Tat functionality and translocon assembly. Results indicate that both components tolerate smaller shortenings or extensions, but the natural 12 consecutive hydrophobic residues appear to function best. We demonstrate that, in case of TatB, this hydrophobic mismatch is important for the stable interaction of TatB with TatC, and therefore the short helices most likely trigger also the association of TatA with TatBC. To also analyze potential effects on the so far uncharacterized larger TatA assemblies that are present at Tat translocons during the translocation cycle, we visualized and characterized such assemblies in whole cells by metal-tagging transmission electron microscopy (METTEM), which to our

knowledge is the first direct visualization of membrane protein interactions in whole cells, and then carried out molecular dynamics (MD) simulations. As a result of these simulations, we found that the short length of the TMH, together with the APH, has the potential to locally thin and destabilize the membrane. This is expected to cause membrane stress, which we could experimentally confirm by the analysis of the Psp membrane stress response induction.

Our study gives a biochemical and structural explanation for the membrane destabilization that is locally generated at Tat systems to permit the transport of folded proteins in all domains of life. The strictly conserved length of the TMH in TatA and TatB is not an obligate functional requirement and rather represents a compromise between a mechanistically important membrane destabilization and membrane stress minimization.

Results

Tat systems tolerate some shortening and extension of the stretch of 12 consecutive hydrophobic residues in the TMHs of TatA and TatB

To analyze the potential role of the short stretch of 12 consecutive hydrophobic residues in the TMHs of TatA and TatB, we shortened the hydrophobic helix by removing 1, 3, 5, or 7 residues in TatA, and 1 or 3 residues in TatB. We also extended the helix by 1, 2, 3, 4, 5, 6, or 7 leucine residues in TatA, and by 3 or 4 leucine residues in TatB (Fig. 1*B*). In the following, the nomenclature of the constructs is facilitated for the reader, with "A+1" standing for the construct with one Leu inserted into the helix of TatA and "B-3" standing for the construct with three hydrophobic residues deleted in the helix of TatB, as examples. To ensure the correct ratio of the Tat proteins, all genetic constructs were generated with the *tatABC* operon under control of its natural promoter in the Tat complementation vector pABS-*tatABC* (39). We used the *tat*-deletion strain DADE (40) in combination with these vectors, which permitted functional analyses as well as Blue-Native Polyacrylamide Gel Electrophoresis (BN-PAGE) detections of the Tat complexes. All TatA and TatB variants were stably produced, and carbonate washes revealed that all of them were membrane-integrated (Fig. 1*C*). The membrane integration of the very short TatA membrane anchors, such as A-5 or A-7, was unexpected and can only be explained by a major contribution of the APH. As expected, a significant portion of all TatA variants was released from the membranes, which is already known for TatA and may be due to the presence of these proteins in destabilized membrane regions (25). The shorter the membrane anchor, the more TatA was released by carbonate washes, indicating that membranes could not stably retain these TatA variants, possibly due to local membrane weakening (Fig. 1*C*, compare A-1, A-3, A-5, and A-7). As TatA can destabilize membranes, these results may indicate that shorter membrane anchors enhance the membrane-destabilizing effect of TatA. TatB and its variants were more stably membrane-integrated, which is expected as TatB tightly associates with TatC. We then analyzed Tat functionality with the described Tat systems. As Tat-deficient strains become SDS-sensitive, which relates to cell wall defects due to Tat-requirement for transport of the cell wall amidases AmiA and AmiC (41), we assessed Tat functionality by monitoring SDS resistance of the respective strains (Fig. 2*A*).

Only the A-5 and A-7 constructs were inactive among the TatA variants with shortenings, and only the A+6 and A+7 constructs were inactive among the extension variants. The A-5 and A-7 deletion variants showed higher sensitivity toward SDS than the noncomplemented *tat* deletion strain, indicating that these variants were not only nonfunctional but also had an additional negative physiological effect.

In case of TatB, the B-1 and B-3 deletion variants were both active in this assay, indicating that shorter hydrophobic helices in principle suffice to establish functional Tat translocons. This was unexpected as TatB tightly interacts with TatC for function, and we therefore expected less tolerance. The Tat system also tolerated the 3-residues extension in TatB but not anymore the 4-residues extension. As TatA and TatB possibly could have overlapping functions and therefore could complement defects of each other, we also tested combinations of single and triple deletions in TatA and TatB and triple extensions in TatA and TatB. Notably, the combined deletions were functional, indicating that indeed the deletions did not inactivate the proteins. The combined extension (A+3/B+3) showed a markedly reduced SDS resistance, indicating that some functional overlap had masked the effect of single +3 extensions. Nevertheless, the partial SDS resistance proofed residual activity of A+3 and B+3 variants.

A second way to monitor functionality is the chain formation phenotype, which is similarly based on the absence of AmiA and AmiC in the periplasm of Tat-deficient strains. If these amidases are not transported into the periplasm, the murein is not efficiently hydrolyzed between separating cells, resulting in chains of cells. In full agreement with the SDS-sensitivity measurements, the chain formation phenotype was only observed in those strains that were also SDS-sensitive (Fig. 2*B*). The strain with the A+3/B+3 combination, which had reduced but not abolished SDS resistance, showed no chain formation phenotype, indicating that sufficient amidases were transported for cell separation and confirming the residual activity of the Tat system with the +3 extensions in TatA and TatB. In line with that, the SDS-sensitive B+4 strain showed no obvious chain formation, indicating that transported amidases sufficed for cell separation but not for SDS resistance.

To recognize weaker effects on protein transport, we then carried out biochemical analyses of the transport of the Tat model substrate HiPIP, which is an iron-sulfur cluster–containing protein that strictly requires the Tat system for transport (15). Subcellular fractions were prepared from exponentially growing cells and analyzed by SDS-PAGE/Western blotting using antibodies specifically recognizing HiPIP (Fig. 3). We used a vector for low-level constitutive HiPIP production, which results in complete translocation of HiPIP into the periplasm in case of fully functional Tat systems (42). In this assay, the mature periplasmic HiPIP band

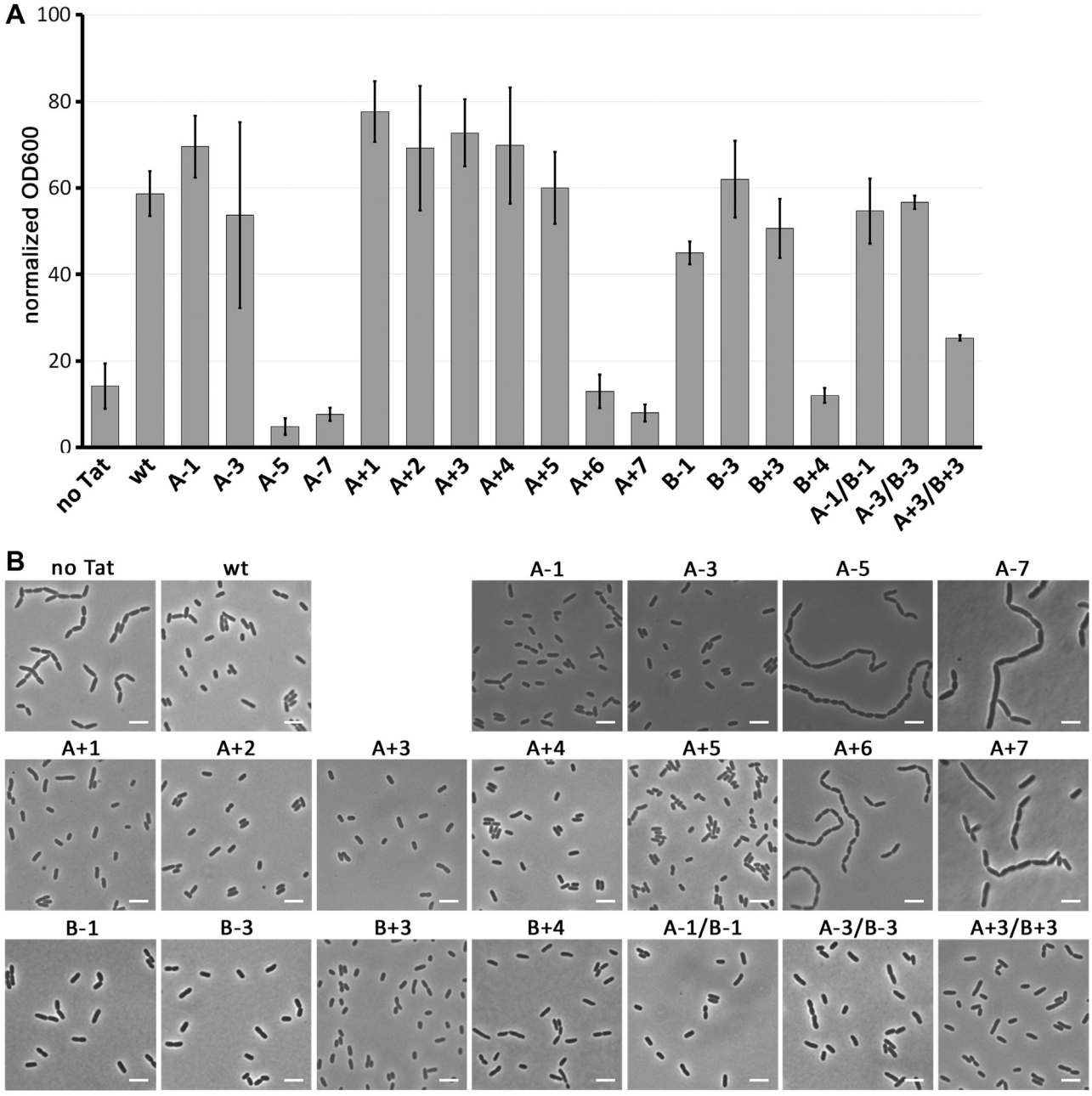

Figure 2. Physiological Tat functionality assays with mutated Tat systems. Complementation of SDS sensitivity (*A*) and chain formation (*B*) phenotypes of the Tat-deficient strain DADE by Tat systems with indicated single or combined TatA and TatB variants. Scale bars in the micrographs correspond to 5 μm. Error bars of the SDS-sensitivity assays indicate SDs as deduced from three or more technical replicates. Controls: 'no Tat', empty vector control; 'wt', WT Tat system.

indicates transport, and any precursor in the cytoplasm indicates reduced translocation relative to the fully functional Tat system. The WT Tat system, which served as positive control, showed a strong band of transported mature HiPIP in the periplasm and no accumulation of precursor in the cytoplasm. Fractionation controls showed that there was no leakage of cytoplasm into the periplasmic fraction, and the only faint mature HiPIP band in the cytoplasm indicated little proteolytic cleavage of the signal peptide or residual periplasm in the cytoplasmic fraction. The Tat-deficient empty vector control strain did not show any transport and instead the bands that are indicative for cytoplasmic accumulation of HiPIP, which are a strong cytoplasmic precursor band and a band that is due to partial degradation of the signal peptide. All TatA variants with shortenings showed detectable cytoplasmic precursor bands, with only very little precursor accumulating in A-1 variants and larger quantities accumulating in A-3 variants. The A-5 and A-7 variants were inactive, with no detectable mature protein in the periplasm. The TatA variants with extensions showed only slightly less transport in the A+1 variant and only very little cytoplasmic precursor in the A+2, A+3, and A+4 variants, but a sudden almost complete block of transport with the A+5 variant. The A+6 and A+7 variants were inactive. With the TatB variants, we observed little

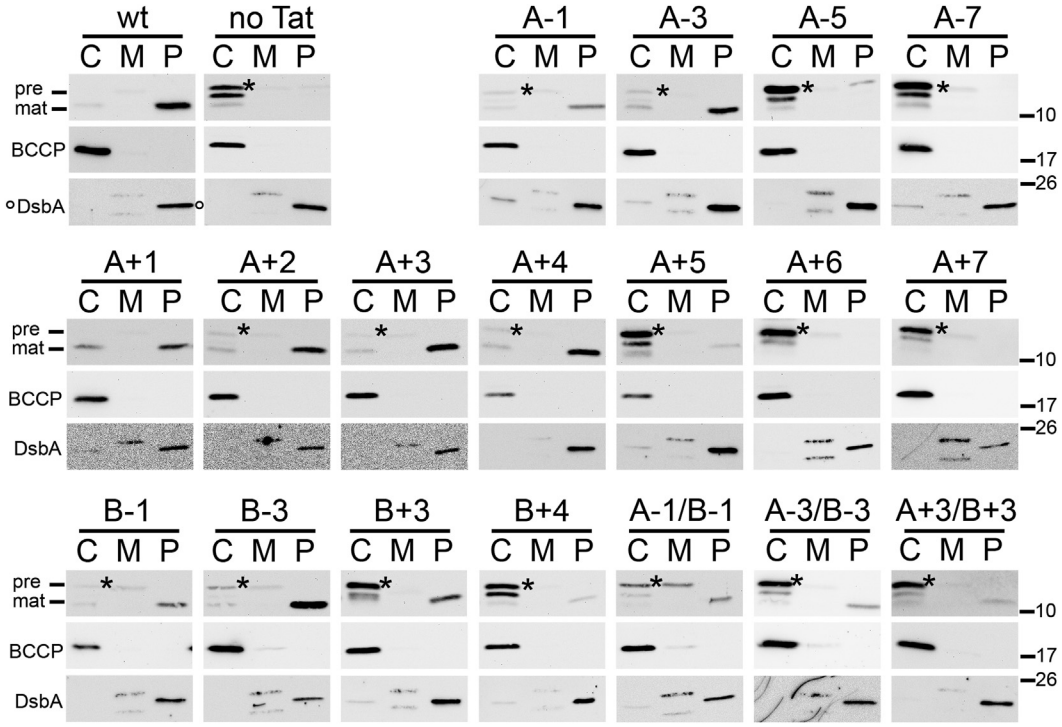

Figure 3. Biochemical Tat functionality assays with mutated Tat systems. Transport analysis by SDS-PAGE/Western blot detection of the precursor (pre, band at 14 kDa) and mature (mat, band at 11 kDa) forms of the Tat substrate HiPIP in subcellular fractions of cells containing the indicated single TatA or TatB variants or combinations thereof (*upper blots*). Biotin carboxyl carrier protein (BCCP, band at 20 kDa) was detected as cytoplasmic fractionation control, and DsbA (band at 21 kDa, marked by a *circle* in the first blot) as periplasmic fractionation control (*lower blots*). Positions of molecular weight markers (kDa) are indicated on the right side of identical blot sections. Cytoplasmically accumulating precursor is marked by *asterisks*. Note that any detection of mature protein in the periplasmic fraction indicates functional transport, whereas accumulation of precursor in the cytoplasm is only observed in cases of a partial or complete defect in transport. C, cytoplasm; M, membrane; P, periplasm.

accumulation with the B-1 and B-3 variants, indicating only a minor defect, whereas the B+3 variant strongly accumulated HiPIP in the cytoplasm and the B+4 variant hardly transported HiPIP anymore. Interestingly, the combinations A-1/B-1, A-3/B-3, and A+3/B+3 all showed a stronger effect than the single variants, indicating that the defects were additive or that there was indeed some partial compensation of defects of TatA by TatB or vice versa detectable in this semi-quantitative assay. Such effects were more difficult to detect by the apparently less-sensitive amidase-based assays, in which few transported enzymes may often suffice for physiological complementations (compare with the SDS sensitivity assay in Fig. 2*A*).

Together, the activity measurements indicate that the 12-residues length of the hydrophobic helix in WT TatA and TatB results in highest transport efficiency. In case of TatA, shortenings by up to three residues and extensions by up to four residues are tolerated, and some residual transport is even detectable with a five-residues extension. TatB similarly tolerates shortenings and truncations of three residues, with only little residual transport detectable in case of the four-residues–extended B+4 variant.

Variation in the TatB TMH length, not in the TatA TMH length, interferes with TatBC complex stability

It is well described that TatB interacts with the short helix 5 of TatC, whereas TatA can interact with the similarly short helix 6 of TatC (28, 36). It was therefore possible that functional effects of length variations in the hydrophobic TMH of TatA or TatB are simply due to disturbed interactions with TatC. To examine this aspect, we analyzed the stability of the known TatC-containing complexes (27).

Membrane fractions were solubilized by digitonin and analyzed by BN-PAGE/Western blotting to detect Tat complexes TC1 and TC2 (Fig. 4). While the complexes were unaffected by the length variations in TatA (Fig. 4*A*), the B+3 and B+4 variants caused disassembly of the complexes (Fig. 4*B*). In case of B-1, only the TC2 band was affected and changed to a very diffuse band, whereas the TC1 band remained unaffected. With B-3, the diffuse band of the size of TC2 was the only remaining complex, and TC1 had completely disappeared. Some disassembly of Tat complexes is always observed and has been described previously (15). Some aggregated or not fully solubilized material is usually observed that remains at the top of the separating gel (17). Together, these data clearly indicate a severe effect of the TatB variants on TatBC interaction and consequently on TatBC complex stability. As also the functional TatB variants showed this destabilizing effect, sufficient TatBC complexes must have been present in living cells to support Tat transport with this expression system.

METTEM-analysis of TatA clusters in the cytoplasmic membrane at WT expression level

In the above shown BN-PAGE analyses, we could only detect effects of TatB variants on the Tat complexes, which is not surprising as most TatA dissociates from the detectable

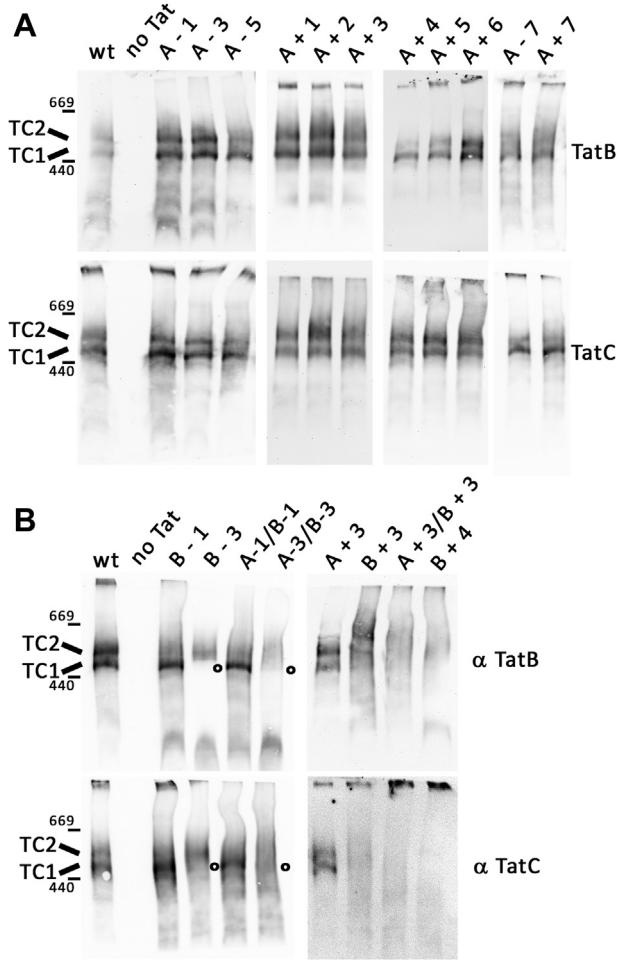

Figure 4. Analysis of Tat complexes in strains with mutated Tat systems. *A*, BN-PAGE/Western blot detection of Tat complex 1 (TC1) and 2 (TC2) in strains containing Tat systems with indicated TatA variants (*A*) or with TatB variants alone or in combination with TatA variants (*B*). Blots were developed with antibodies against TatB (*upper blots*) or TatC (*lower blots*). The position without the TC1 band in B-3 Tat systems is highlighted by *open circles*. B+3 and B+4 extensions have more general destabilizing effects. For direct comparison, the A+3 system is analyzed in parallel with B+3 and the A+3/B+3 combination. Positions of TC1, TC2, and molecular weight markers (440 kDa, 669 kDa) are indicated on the *left*.

TatBC-containing complexes upon detergent solubilization, and only a regular ladder of multiple homooligomeric TatA associations is detected that does not permit analyses of the TatBC-bound TatA (31, 32). To reveal potential effects of the mutations on TatA, the lack of structural information in principle could be overcome by MD simulations. However, to create a reasonable starting point for MD simulations, we required some information about the organization of the large TatA assemblies at translocation sites. So far, it is only known from thylakoidal cross-linking analyses that at least up to 16 TatA protomers can be cross-linked at active translocation sites over a 4-min time span (22), which is evidence for an association of this number of protomers. Another analysis had indirectly calculated a median of 25 interacting TatA-YFP protomers in such complexes, based on mobility and fluorescence intensity measurements (23). The pixel size of 50 nm in these analyses certainly could not resolve single protomers or even whole TatA assemblies. We thus first aimed to examine the proposed larger TatA associations in the *E. coli* system by a higher-resolution method. To our knowledge, electron microscopy is the only currently available technique that can give sufficient positional resolution within cells. We chose MET-TEM for these analyses, using metallothionein-gold tags (43–48). Metallothionein-gold tags have the advantage of directly labeling the protein of interest with rather small electron microscopy–detectable electron-dense domains. In initial experiments with abundant recombinantly produced Tat systems, we found that three metallothioneins in row (= MT3) permitted clearly visible electron-dense granules of ± 1 nm in diameter in *E. coli* cells, and the detected particles could be identified as gold by Parallel Electron Energy-Loss Spectroscopy (PEELS) analysis (Fig. 5). Note that the recombinant protein levels that have been used for the PEELS analysis resulted in large clusters of interconnected associations that sometimes deformed the membrane, but this measurement only served to proof that the gold label of the MT3 tags had worked, and no other conclusion is drawn here.

Having the method established, we attempted to localize the Tat components at WT expression levels in strains that had the modified *tat* operons chromosomally integrated. With TatB-MT3 and TatC-MT3, no gold was detectable at WT level, but it was possible to detect TatA-MT3 in these experiments, which is likely due to the higher abundance of TatA relative to TatB and TatC in *E. coli*, which are present in an estimated 50:2:1 ratio, respectively (49). The WT level of the TatA-MT3-abundance was confirmed by SDS-PAGE/Western blot analysis (Fig. 6*A*). Substrates interact with the cytoplasmic face of TatA (25), and it is known that YFP tags (ca. 26 kDa) at the cytoplasmically located C-terminus of TatA inactivate TatA in the TatABC system of *E. coli* when produced at WT level (21). Similarly, we found that our MT3 tag (ca. 21 kDa) rendered TatA almost inactive, as a slight activity was likely due to some degradation to mature size (Fig. 6*B*). As there so far do not exist any protein tags that can be fused to TatA without compromising activity at WT levels, this result was not surprising. Importantly, the tag did not prevent TatA–TatA interactions, and the number of TatA protomers in these associations was comparable with the number concluded from cross-linking of active nontagged TatA (see below, 22). Therefore, the effect on activity was most likely due to steric inhibitions of substrate interactions, as substrates need to pass through the TatA assemblies. In any case, these analyses can be taken as first direct visualization of WT level TatA assemblies in any organism.

TatA-MT3 formed gold assemblies near cell poles of irregular shape when seen in quasi top-view projection and roughly normal to the electron beam (Fig. 6, *C* and *D*). The mean length of the gold-assemblies was 20 nm ± 6.0 nm (N = 40, min = 10 nm, max = 37 nm). The width of the assemblies was about 10 nm. To determine the number of TatA-MT3 protomers in such assemblies, we counted the number of MT3-gold particles in 35 regions containing MT3-gold and calculated from this the average number of 17 ± 6 MT3-gold particles per 200 nm^2, which is the dimension of an average TatA-MT3 assembly. Interestingly, several of these assemblies visually appeared to be

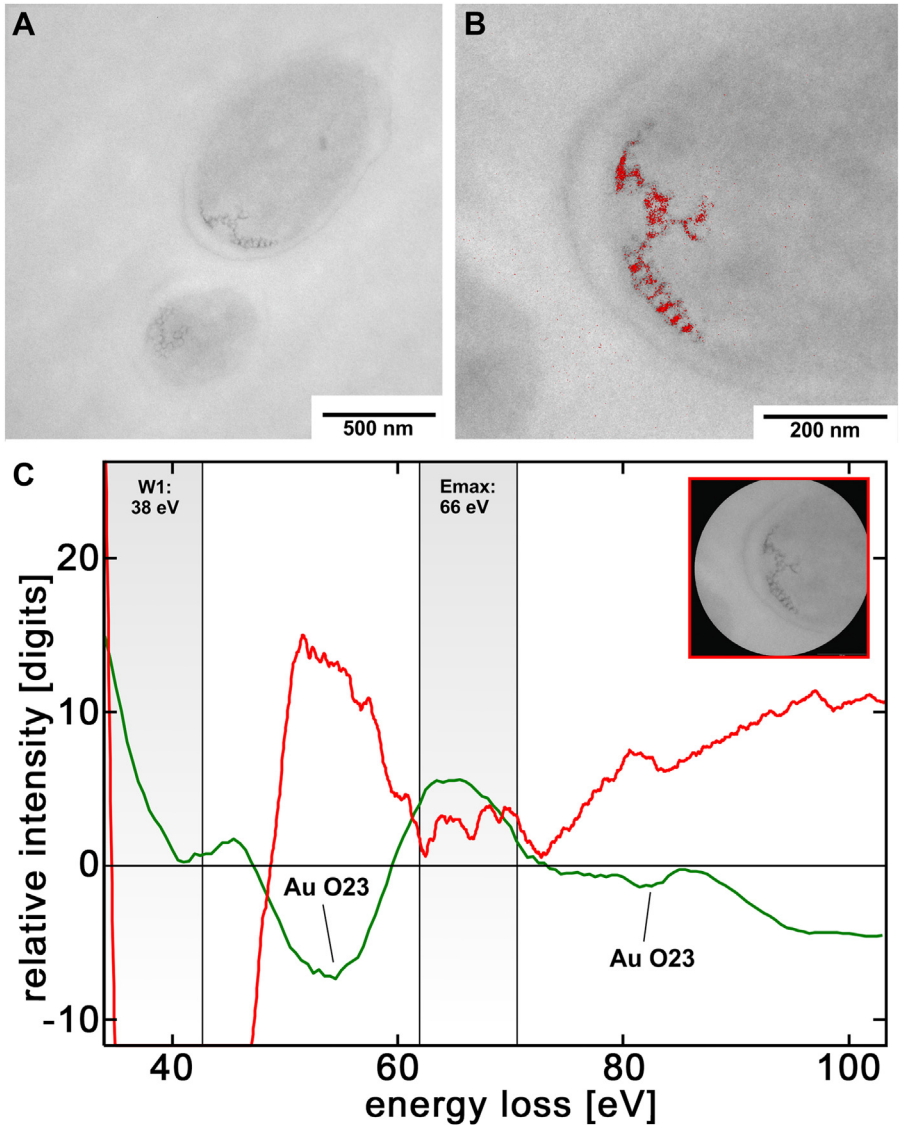

Figure 5. PEELS analysis of TatB-MT3-gold. *A*, survey micrograph of the analyzed cell containing the recombinant TatAB(MT3)C system as expressed by pABS-*tatAB(MT3)C*, with TatB-MT3-gold visible in clusters at the cell pole. *B*, electron spectroscopic element map at the Au-O_{23} edge E_{max} at 66 eV, energy-slit width: 8 eV, superimposed in *red* to a higher resolution image of the cell pole shown in (*A*). Energy-settings and corresponding energy-slit width for the jump-ratio acquisition are indicated in *C* (W1; E_{max}). *C*, PEEL-spectrum of the MT3-gold–containing cell pole shown in (*A*) and (*B*) (inset: measuring area; the *edge length* of the square around the measuring area corresponds to 700 nm), detecting gold at the Au-O_{23} edge (*red graph*) and an energy maximum, which is in accordance to the Au-reference PEELS (*green graph*) from the EELS-atlas (90). PEELS, Parallel Electron Energy-Loss Spectroscopy.

in contact, suggesting that they were somehow interdependent or connected (Fig. 6, *E–H*), which might be due to a clustering with TatBC complexes. Note that the MT3-gold intensity was variable, most likely due to individual kinetics of gold aggregate formation within MT3 tags, which may depend on the local environment (Fig. 7, *A–C*). Sometimes, TatA-MT3–gold-assemblies appeared in longer linear arrangements in the membrane. However, tilting of the sample revealed these arrangements to result from the superposition of individual assemblies when they are oriented in parallel to the electron beam within the ultrathin section (Fig. 7*D*).

In conclusion, TatA-MT3 formed longitudinal assemblies of irregular shape that were usually positioned near cell poles, the subcellular location of Tat translocons that has been observed in previous fluorescence-based studies (20, 50). The number of subunits in such assemblies agreed with previous calculations (22, 23). An often observed close clustering of several of these TatA assemblies suggested their indirect interaction, possibly mediated by TatBC, which explains the previous detection of a significant number of larger associations by fluorescence microscopy that was limited to 50 nm pixel resolution (23).

MD simulation indicates membrane thinning and lipid disorder generation by the short TMHs and aligned APHs of TatA clusters

Based on the METTEM analyses, which had directly shown the interacting TatA protomers and their predominantly linear

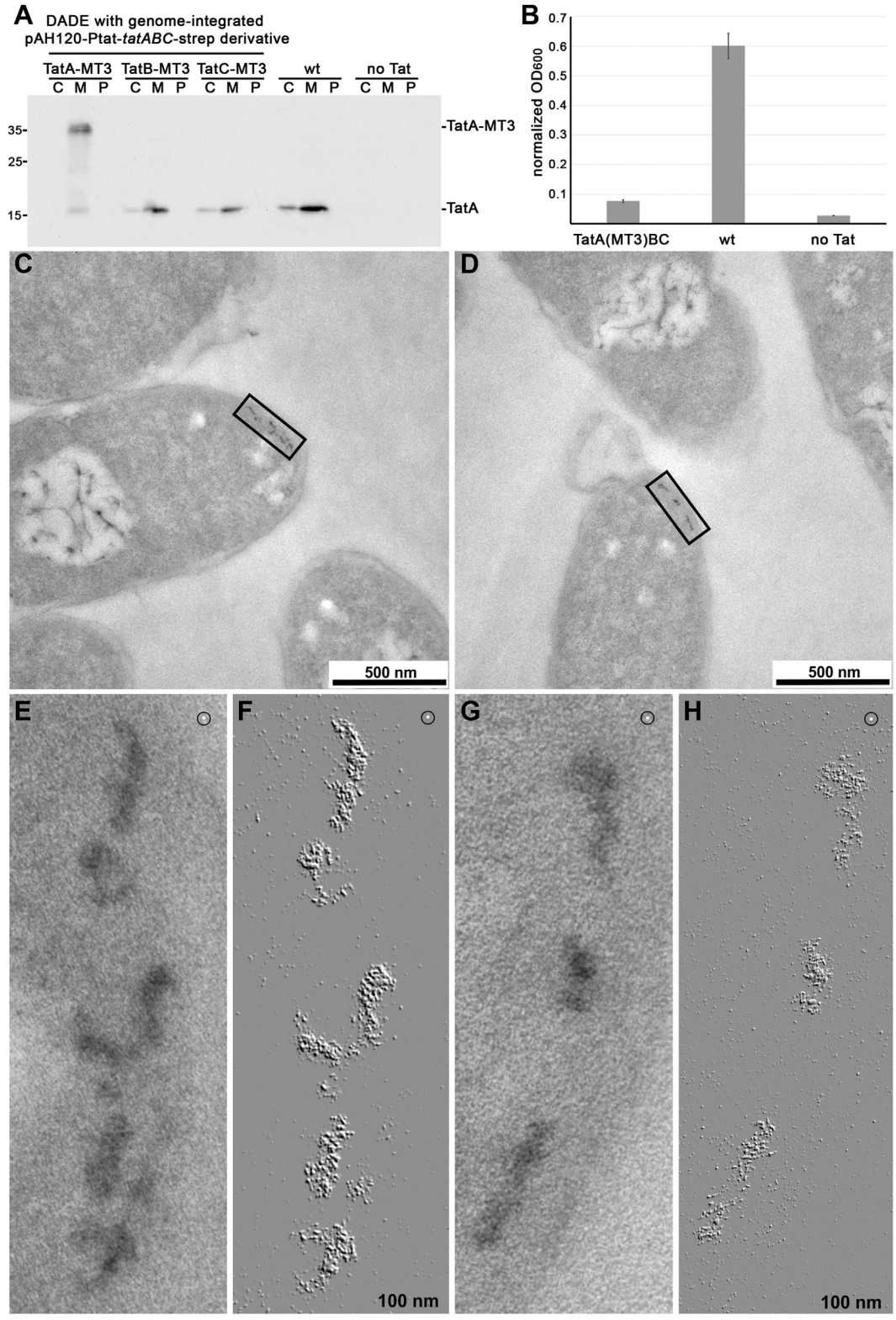

Figure 6. Detection of TatA-MT3-gold at WT expression level. *A*, detection of TatA by SDS-PAGE/Western blot analysis in subcellular fractions of strains with MT3-tags at TatA, TatB, or TatC as encoded by single copy chromosomally integrated *tatABC-strep* operons. WT *Escherichia coli* and the Tat-deficient strain DADE are analyzed for comparison. Positions of molecular weight markers are indicated on the *left*. *B*, SDS-sensitivity measurements of strains with TatA(MT3)BC, TatABC (wt), or no Tat system. *C–H*, clusters of TatA assemblies at WT expression level in strain DADE with a chromosomally integrated *tatA(MT3)BC* operon. (*C* and *D*) show overview images of cells with gold-labeled TatA-MT3-assemblies. *Areas boxed* in the respective overviews are shown in (*E* and *H*) at higher magnification. (*E* and *G*) are original images, and (*F* and *H*) were topographically 'relief'-filtered to discriminate MT3-gold granules in pseudo-3D within TatA-MT3 assemblies (*lower edge* = 100 nm). *White* 1 nm-dots (encircled in *C–F*) have been included as a direct scale for 1 nm MT3-gold-granules. C, cytoplasm; M, membrane; P, periplasm.

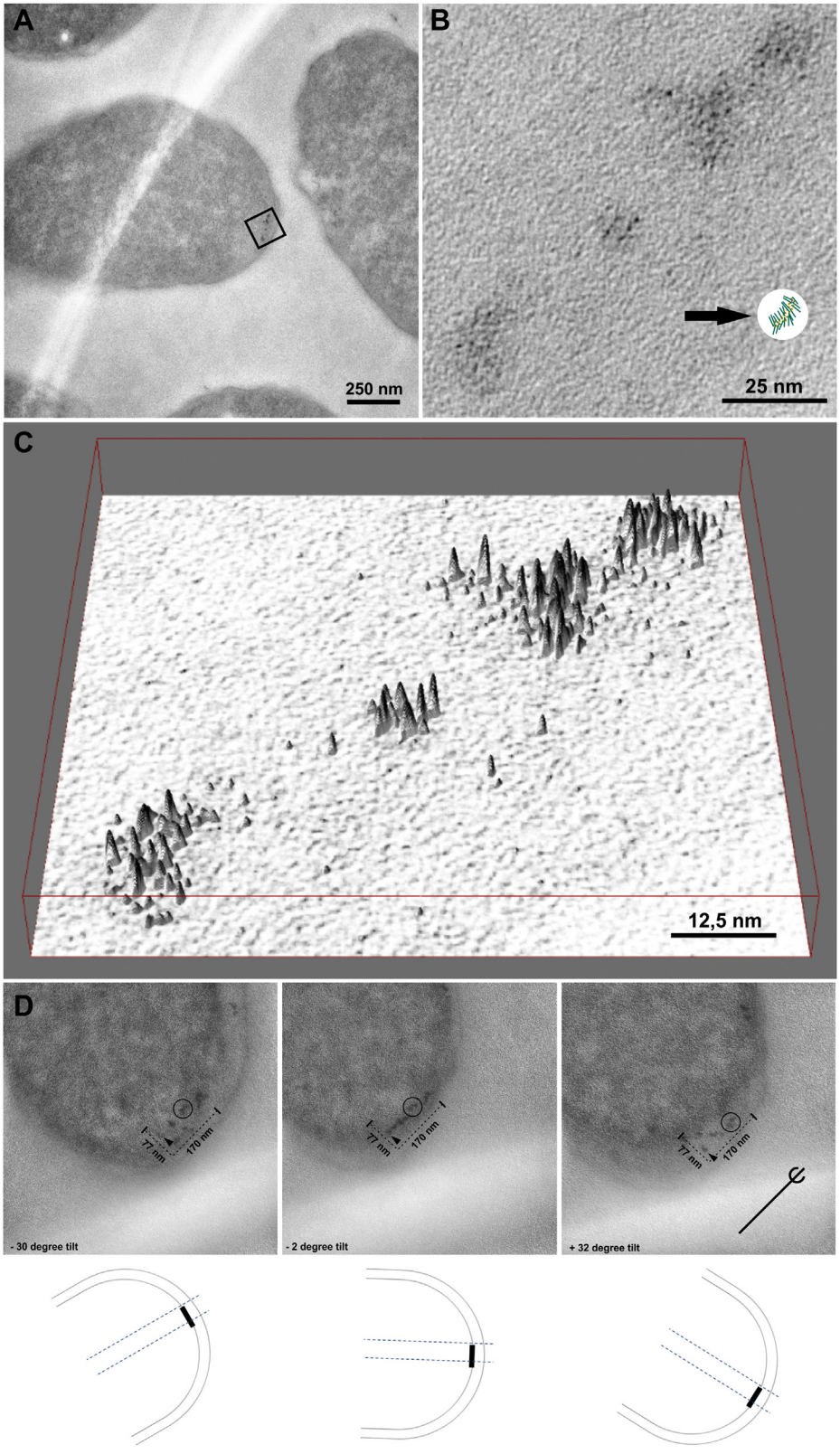

Figure 7. Detailed qualitative aspects of TatA-MT3-gold–labeled assemblies in *Escherichia coli* at WT level. *A*, survey view of an individual cell with a TatA-MT3 cluster, labeled with electron-dense gold (*squared frame*) in the subpolar region. *B*, detailed view of the area framed in (*A*), showing the TatA-MT3 assemblies of the cluster at higher magnification. Note the electron-dense granules of individual TatA-MT3-gold tags, which are about 1 to 1.5 nm in size. An isoscale scheme of the MD-simulated TatA assembly of 22 protomers (*arrow*, see Fig. 8*A*) is included for comparison. Note that the MT3 domains are 69 residues apart from the modeled APHs (*green*). *C*, a tilted, 3D-surface plot shows the range of *gray* level variance above the cytoplasmic background within the assemblies, which is indicative for MT3-gold. High peaks with *black caps* represent gold granules, as they can be readily recognized in (*B*). The range of different peak heights from *high to low* as seen in (*C*) indicates a variability of gold-loading of MT3 tags during the incubation of the cells with tetrachloroauric acid, possibly caused by differences in the local environment and unequal accessibility of gold. *D*, TEM-Tilting analysis of polar TatA assemblies.

assemblies, we were able to carry out 1500 ns MD simulations with 22 TatA protomers in the cytoplasmic membrane lipid bilayer, which is in the upper range of the observed TatA assemblies and therefore might reflect functional associations at Tat translocons. The MD simulations were challenged by the fact that, in living cells, larger TatA assemblies require TatBC interactions for their formation (20, 21). As no TatBC complex structure is known, and as we therefore could not include TatBC complexes in the simulations, we attempted to overcome this problem by placing linear arrangements of TatA protomers in close proximity with opposite APH-orientation. We had four reasons to expect a linear arrangement of TatA in the TatA assemblies: (1) our METTEM analyses had detected longitudinal assemblies (see Fig. 6), (2) an NMR structure of a TatA dimer showed laterally aligned APHs, which is only possible in linear arrangements (10), (3) circularly arranged TatA protomers had been reported to collapse within 40 ns in MD simulations, unless the circles were filled with a lipid bilayer that would need to be removed to permit translocation (8), and (4) a linear arrangement would permit regular interactions between TMHs of two oppositely oriented TatA protomers. This approach was successful, as the TMHs readily moved into staggered positions, and the resulting complex remained stable over time in the 1500 ns simulation (Fig. 8). Most APHs laterally contacted neighboring APHs, with some interactions interrupted (Fig. 8*A*), which agrees with the NMR evidence for lateral APH association (10), and these aligned APHs formed an angle of in average 109° with the TMH, which agrees with solid state NMR analyses on *Bacillus subtilis* TatA (51).

Also, the hinge was positioned deep in the membrane, which agrees with accessibility analysis data (25). The aligned APHs formed a deep V-shaped groove at the membrane surface (Fig. 8*B* and Video S1). As a result of this constellation, the membrane was thinned to about half its natural thickness at the hinge region. A view on the lipids in this simulation revealed that the lipid head groups were excluded from areas of aligned APHs, and the acyl groups were therefore disordered and partly oriented in parallel to the APHs. The lipid disorder in the membranes could be quantified employing the lipid tail order parameter S_{zz} (Fig. 8*C*). The data confirmed that the lipid order was lowered in the environment of the APHs.

We then carried out the simulations with the TatA variants A-5, A-3, A-1, A+1, A+2, A+4, and A+6. As now expected, the shortenings resulted in further thinning of the membrane, whereas the extensions of the TMH resulted in a thicker membrane, which becomes evident when comparing the simulations A-5, wt, and A+6 (Fig. 8*B*). Accordingly, the lipid order further decreased with a shorter TMH and increased with a longer TMH (Fig. 8*C*). The TatA simulations therefore had added a potential new aspect to the role of the short length of the TMH, as they suggested that this exact length might not only be relevant for interactions (as shown for TatB; see Fig. 4) but also for membrane destabilization, which mechanistically could be important (see Discussion).

As the MD simulations had indicated that large TatA assemblies can thin the membrane, we addressed whether the number of TatA protomers in the association could be relevant for membrane thinning. We repeated the simulations with 15, 10, and 5 TatA protomers and found that the membrane-thinning effect required the lateral association of multiple APHs, which was the reason why only associations of >10 TatA protomers efficiently formed the V-shaped groove in the membrane (Fig. 9, *A* and *B*). In case of only five protomers, the lateral associations of APHs were too few to impose a V-shaped groove on the membrane lipids, which is why such small associations had less effect on the membrane bilayer, as quantified by the tail order parameter (Fig. 9*C* and Video S2).

Changing the length of the TatA TMH can affect cellular growth

The MD simulations suggested a second potential reason for the exact TMH length, which is the compromise between a mechanistically required membrane destabilization and an energetically required membrane stability. It has already been shown several years ago in *in vitro* experiments that TatA can destabilize the membrane and substrate-binding to TatA enhances this membrane destabilization, resulting in proton leakage (25). We thus wondered whether a too short TMH could result in extreme membrane destabilization *in vivo*, which could represent a selective pressure for maintaining the minimum of 12 consecutive hydrophobic residues in TatA (and consequently also in TatB and the short helices 5 and 6 in TatC, which need to assemble with TatA at the translocation site). As proton leakage might affect growth, we analyzed growth of all strains used in our study (Fig. 10).

Growth curves indicated a delay of growth by A-5, A-7, A+6, A+7, B-1, and A-3/B-3 systems, which may have been caused by cellular adaptations to stressed membranes (Fig. 10*A*). Some cases, especially A-5, A+6, and A+7, resulted in slow growth, indicating insufficient adaptations and persistent harm. The Psp membrane–stress-response system is most likely involved in the adaptation to the membrane destabilization by the hydrophobic mismatch, as PspA is known to suppress proton leakage (52), and PspA of *E. coli* as well as its homolog LiaH in *B. subtilis* have been shown to interact with Tat systems (53, 54). We therefore tested this and found that shortened and elongated TatA variants as well as the B-1 variant induced the Psp membrane stress response, as monitored by an increase in PspA abundance (Fig. 10*B*). Interestingly, A-3 had a stronger effect than A-5 or A-7, and B-1 had a stronger effect than B-3, indicating that the orientation of the APH relative to the TMH influences stressor sensing by the Psp system. This upregulation represents most

A seemingly very long TatA association, detectable by TEM of TatA-MT3-gold at a cell pole (*middle*), has been analyzed in the same cell by tilting the sample from −30° (*left*) to +32° (*right*). The tilted cell revealed that individual TatA-MT3 gold assemblies had been transformed into a single longer association due to superprojection of the assemblies when oriented parallel to the electron beam (tilt −2°).

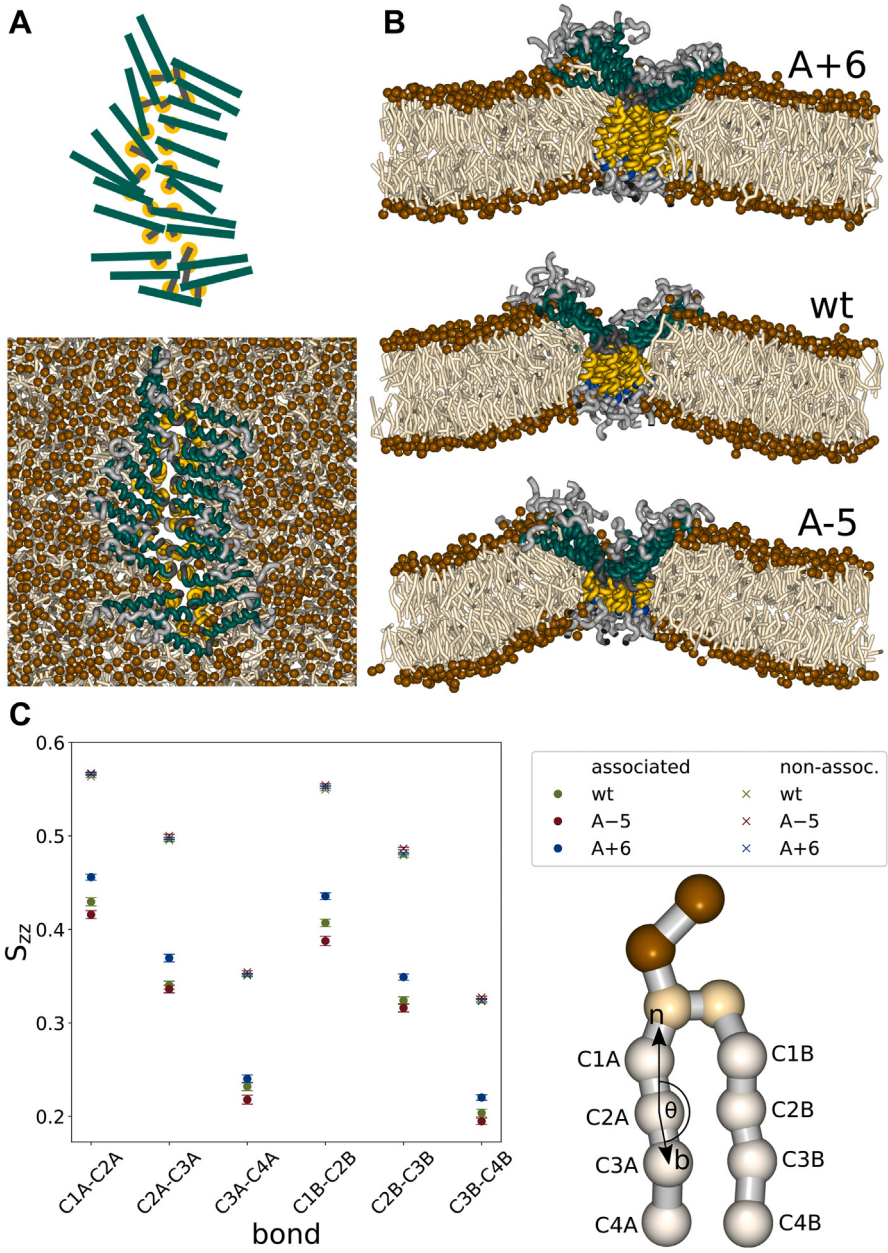

Figure 8. MD simulations with 22 TatA protomers of the WT and the variants A-5 and A+6. *A*, *top view* from the cytoplasmic side on the 22 TatA wt simulation. *B*, cross sections through TatA complexes, with the cytoplasm above and the periplasm below the membrane cross sections. TMH, *yellow*; APH, *cyan*; Q8, *turquoise*; hinge region, *dark gray*; N- and C-termini, *gray*; lipids, *light* and *dark* (head groups) *brown*. *C*, lipid tail order parameter for lipids in the vicinity of the TMH (associated) and lipids in the bulk phase (nonassociated). Bars indicate 95% confidence intervals. The shown coarse-grained model of DPPE illustrates tail beads and the orientation of an example tail bond vector (b) relative to the bilayer normal (n), which is the basis for the order parameter. The other beads in the model are ethanolamine and phosphate (*brown*), and glycerol (*light brown*).

likely the adaptation that permits normal growth of strain A-3. In contrast, insufficient PspA induction in case of the extremely short A-5 and A-7 constructs most likely caused the clear growth phenotype. As the slow growth of the A+6 and A+7 constructs correlated also with the membrane stress response, this phenotype may be due to proton leakage as result of an influence on structures of other membrane proteins. The B+3 and B+4 constructs, which had a strongly reduced activity (Figs. 2 and 3) due to a diminished TatC interaction (Fig. 4), did not cause any significant growth phenotype, as the TatB elongations did not cause membrane destabilization (Fig. 10*B*). In general, constructs that did not have much effect on activity or whose effect on membrane stability could be compensated by the membrane stress response did not have strong effects on growth (Fig. 10), indicating that not compensated membrane stress likely is the reason for the observed growth phenotypes.

Dominance of nonfunctional TatA variants

To examine whether the inactive TatA variants influence the activity of functional Tat translocons, we examined Tat transport of the tat WT strain MC4100 in the presence or

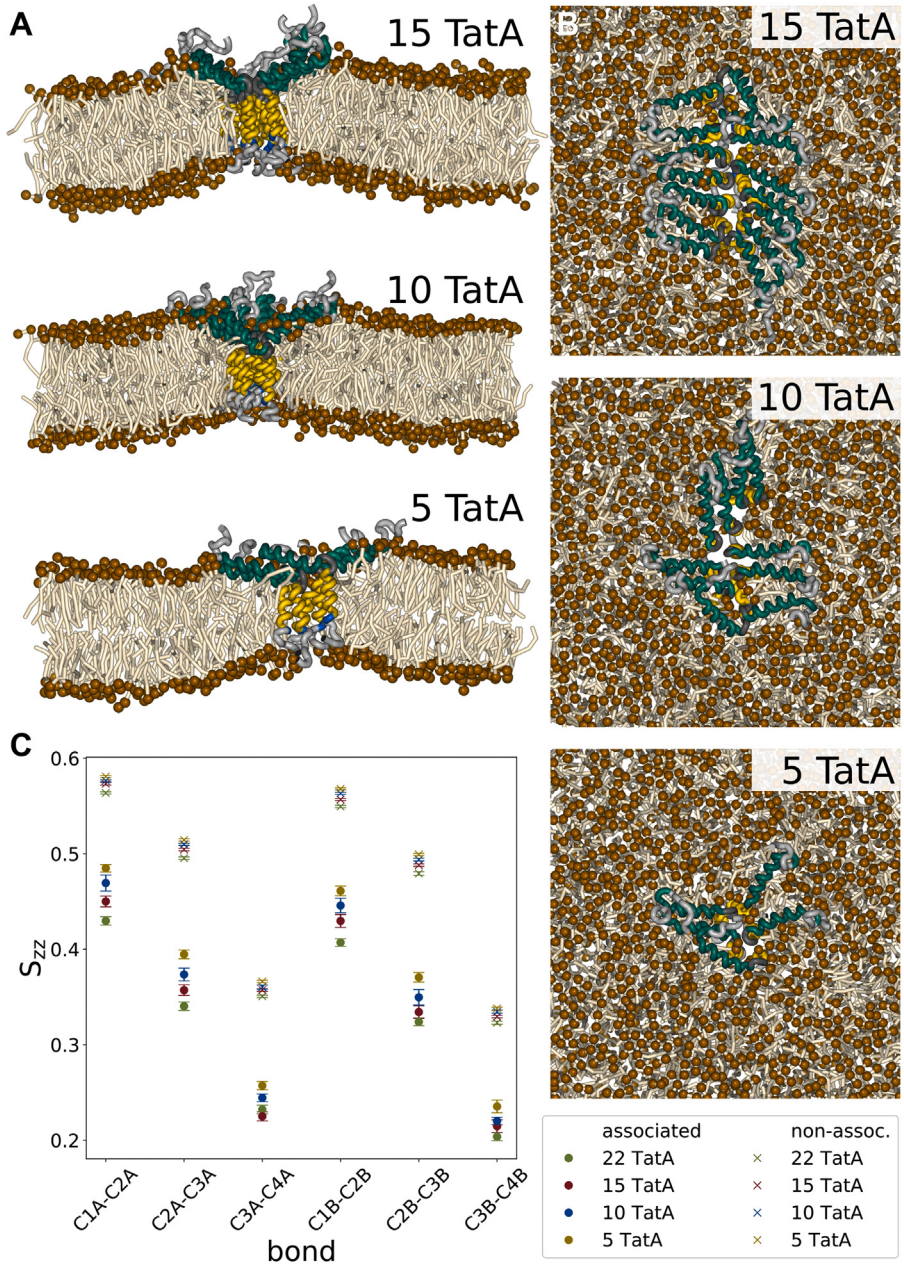

Figure 9. MD simulations with TatA complex of 15, 10, and 5 protomers. *A*, cross sections through TatA complexes. TMH, *yellow*; APH, *turquoise*; Q8, *blue*; hinge region, *dark gray*; N- and C-termini, *gray*; lipids, *light* and *dark* (head groups) *brown*. *B*, *top views* on the TatA complexes. *C*, lipid tail order parameter for lipids in the vicinity of the TMH (associated) and lipids in the bulk phase (nonassociated). Bars indicate 95% confidence intervals.

absence of the recombinant inactive Tat systems A-5, A-7, A+6, and A+7 (Fig. 11). A microscopic examination already indicated that the recombinant A-5 Tat system suppresses Tat transport by the WT system of MC4100 (Fig. 11*A*). The more sensitive HiPIP transport assay then clearly showed that Tat transport is significantly inhibited in all four strains (Fig. 11*B*). In combination, these two assays indicate that the four tested nonfunctional TatA variants most likely mix into functional Tat systems, thereby rendering them almost inactive. The A-5 variant has the strongest inhibitory effect, resulting even in a chain-formation phenotype, whereas the residual activity suffices to enable normal cell separation in the other three cases. We also analyzed the induction of the Psp membrane stress response in these constructs (Fig. 11*C*). There was already a detectable upregulation by nonmutated recombinant Tat systems in strain MC4100, and this was markedly enhanced by A-5, A-7, A+6, or A+7 Tat systems, with A+7 resulting in the strongest membrane stress response. In summary, inactive TatA variants caused membrane stress also in MC4100 and exerted a dominant negative effect on the active WT Tat system in MC4100, most likely by mixing into the active translocons and thereby reducing their activity.

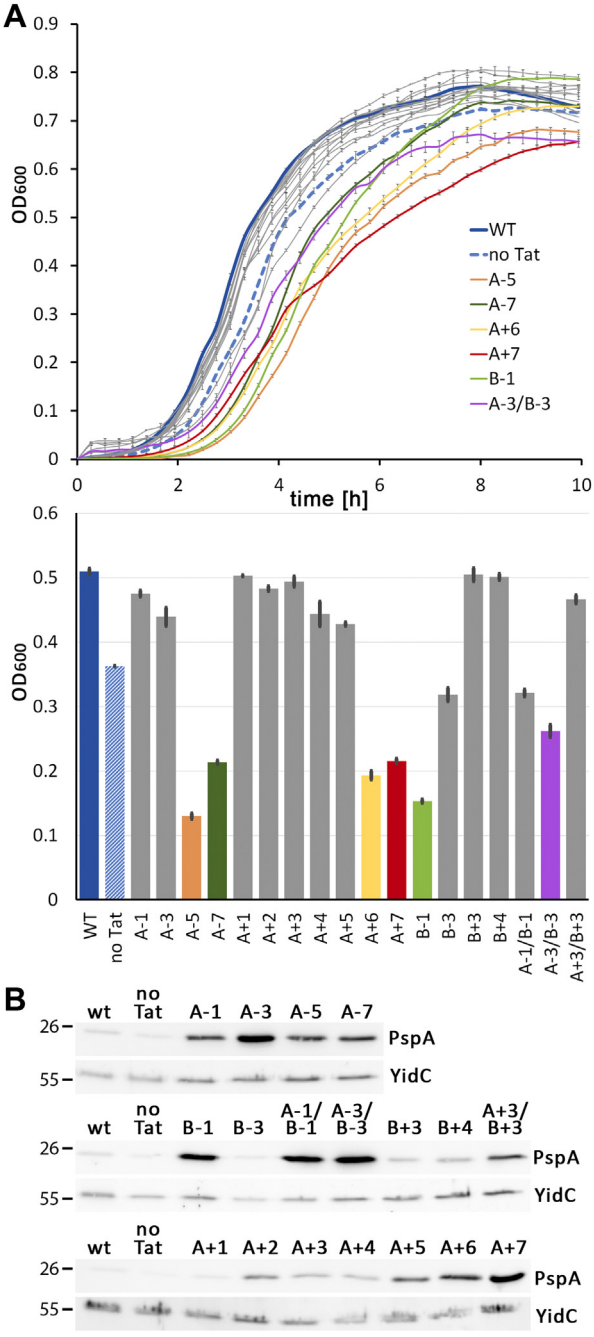

Figure 10. Growth analysis of strains containing the Tat systems analyzed in this study. *A*, A-5, A-7, A+6, A+7, B-1, A-3/B-3 inhibit cellular growth. For comparison, strains with the WT Tat system (wt) and without a Tat system (no Tat) are included in the growth analyses. All curves from constructs with growth in the range between the WT (*blue line*) and the Tat-deficient strain (no Tat, *dashed blue line*) are in *gray* and not specifically labeled for clarity reason. Stronger delayed or diminished growth phenotypes are labeled, and the corresponding curves are colored. Below the growth curves, the growth phenotypes of strains with all Tat systems used in this study are compared, using the OD_{600} at the 3:36 h time point, as this time point is close to the end of the exponential growth of the fastest growing strains. Error bars indicate the SD of technical triplicates. Note that the OD_{600} was recorded by a 96-well multititer plate reader with 5.3 mm initial path length. *B*, SDS-PAGE/Western-Blot detection of PspA (*upper blot*) and YidC (membrane protein control, *lower blot*) in membrane fractions of indicated strains, demonstrating the induction of the Psp response by membrane stress as generated by TMH length variations. Positions of molecular weight markers (kDa) are indicated on the *right side* of identical blot sections.

Discussion

Helices that pass the bacterial cytoplasmic membrane have to traverse a hydrophobic environment of about 3 nm (55). However, the TMH of TatA is predicted to consist of only 15 residues (10) and that of TatB consists of only 13 residues (9), and in these helices, there is only a stretch of 12 consecutive hydrophobic residues. A helix of 12 residues has a length of 1.8 nm, which does not suffice to span a lipid bilayer and therefore causes a hydrophobic mismatch. Such mismatches often have functional implications, such as the regulation of the mechanosensitive channel MscL or the aquaporin GlpF (55, 56), and hydrophobic mismatches can drive membrane protein interactions (57). This study now indicates that hydrophobic mismatches are also important for Tat functionality and Tat component interactions. The length of 12 residues is not a strict requirement for Tat transport but rather an optimal length, as little elongations and extensions of the TMH only reduce but not completely abolish function and interactions (Figs. 2 and 3). In case of TatB, our data show that all length variations affect TatBC complex stability (Fig. 4), and activity reductions are therefore likely due to weaker TatBC interactions. It is interesting that specific variations of the TMH in TatB can have selective effects on the different complexes, which might relate to conformational equilibria of the Tat complexes, such as previously described for mutations in TatC (27). Observations of residual activity with extended or shortened hydrophobic stretches in TatB are suggestive for significant flexibility of interactions within TatBC complexes, which likely are not rigid but rather dynamic oligomers. Also in case of TatA, a compromised interaction with TatB and/or TatC could contribute to the observed transport defects. Interestingly, the combination of extensions or shortenings in TatA and TatB showed more severe defects than the mutations in single components, indicating that there exists some detectable functional overlap between TatA and TatB. The TatA TMH can occupy the same TatC-binding site as TatB (28), which may account for this functional overlap, and as the TatC interaction is likely important also for TatA, length variation in the TMH of TatA is expected to influence activity of the system, as does the length variation in the TMH of TatB.

As BN-PAGE is not helpful to address potential effects on TatA associations, which is due to the multiple associations that TatA forms in the presence of detergent, we sought to model such TatA associations with WT or mutated membrane anchors by MD simulations. Before doing any MD simulation, we required a more direct evidence for oligomeric TatA assemblies in *E. coli*, and the METTEM analysis served that purpose, showing that TatA-MT3 can indeed form large associations of an average 17 ± 6 protomers, which in turn can cluster to even larger associations, suggesting bridging interactions with other components, such as TatBC. In the end, our METTEM data fully agree with the cross-linking data of the thylakoid system, in which interacting components had been trapped over minutes (22), and they are also in remarkable agreement with the mean number of 25 protomers that have been calculated from fluorescence intensity and mobility

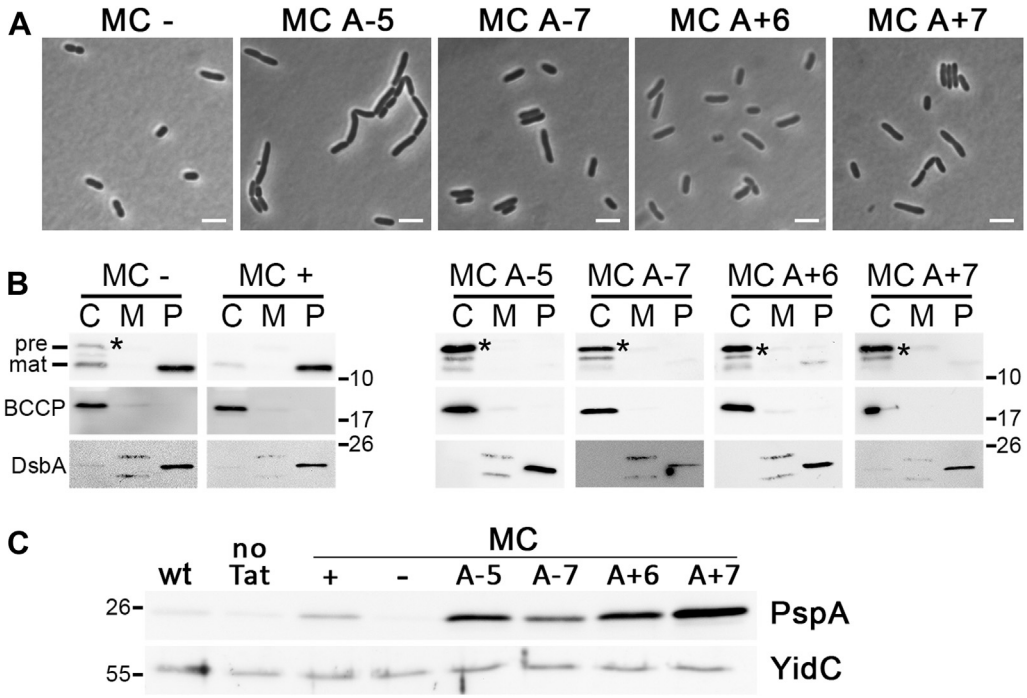

Figure 11. Effects of inactive TatA systems on Tat transport and membrane stress induction in strain MC4100. Influence of indicated Tat systems on cell division (*A*), HiPIP transport (*B*), and membrane stress induction (*C*) in strain MC4100 that chromosomally encodes a functional Tat system. Other strain designations: MC+: MC4100/pABS-*tatABC*; MC-: MC4100/pABS (empty vector); wt: DADE with pABS-*tatABC*, no Tat: DADE with pABS (empty vector). Scale bars in the micrographs correspond to 5 μm. Molecular weight marker positions (kDa) are indicated. See legend of Figures 2, 3 and 10 for more details.

measurements of TatA-YFP foci (23). The latter fluorescence study also reported much larger TatA-YFP associations (at least up to 100 TatA-YFP), which may correspond to the somehow interconnected TatA assemblies in our METTEM analyses. Bridged-TatA assemblies likely diffuse together and therefore were not distinguishable from individual TatA assemblies within the 50 nm pixels in these fluorescence analyses (23). In contrast, METTEM resolved the 1 nm MT3-gold tags and therefore had a higher resolution than the current limit of ~20 nm in super-resolution fluorescence techniques (58). To our knowledge, this is the first application for METTEM in localization of membrane protein associations in any organism.

Having directly seen and characterized WT level TatA associations in cells, we first simulated a larger cluster with 22 subunits, which was well in the size range of typical TatA assemblies in METTEM analysis (Fig. 7) and should be in the range of sizes of TatA associations at TatBC complexes. These simulations readily yielded stable TatA associations, with TMHs interacting with each other on a staggered position (Fig. 8). The assemblies were rather flexible, often showing small kinks due to some irregularities in the arrangements.

Most importantly, the MD simulations revealed that a potential second function of the short TMH could be membrane destabilization. The lipid tail order parameter clearly indicates a correlation of TMH length and membrane destabilization (Fig. 8*C*). Also important is the finding that, in these MD simulations, a larger association of TatAs is required for an efficient membrane destabilization (Fig. 9) and that the generation of the V-shaped groove comes along with generation of membrane curvature (Figs. 8 and 9). The simulations fully agree with published data: the APHs laterally interact, as previously evidenced by NMR (10), the TMHs laterally interact, as suggested by previous spin-labeling electron paramagnetic resonance studies (35), the hinge domain is positioned deep in the membrane, as supported by in fluorescence quencher accessibility studies (25), and the APHs have a tilted orientation in the membrane, as seen in solid state NMR studies with *B. subtilis* TatA (51). It is noteworthy that the average angle of the APH relative to the TMH in the simulations is near 109°, which is in good agreement with the angle determined by solid state NMR (51).

Considering the obvious mechanistic tolerance of some length variation (Figs. 2 and 3), the strict conservation of the short length of 12 consecutive hydrophobic residues in TatA and TatB from bacteria, archaea, and plastids (Fig. 1) is unexpected, especially if only the functionality of protein–protein interactions is assumed to generate the selective pressure for the specific length. However, if membrane destabilization is a second function of these short TMHs, which may be of fundamental importance for the transport mechanism (59), then the hydrophobic mismatch as generated by the strict 12-residue length could be a delicate compromise between transport efficiency and proton leakage. Our MD simulations clearly show that the short TMHs and aligned tilted APHs of TatA have the potential to destabilize membranes, and the simulations of the TatA assemblies with extended or shortened TMHs show clear effects of such alterations on membrane thickness and lipid order (Fig. 8). Proton-tight membranes are of key importance for energy metabolism,

and bacteria have (often multiple) protective systems, which compensate for membrane destabilizations. First growth experiments already indicate that mayor adaptation processes are required in response to A-5 and B-3 systems, and adaptations to minor changes in TMH length on the membrane energetization may be sufficient to suppress growth phenotypes (Fig. 10, *A* and *B*). In agreement with this hypothesis, we found that the Psp membrane stress response was induced by A-3 and A-5 systems, and this induction was much stronger in A-3 than in A-5, which is in agreement with the growth data. The Psp system is known to stabilize membranes (52) and PspA already has been shown to interact with TatA in Tat systems of Gram negative and Gram positive bacteria (53, 54).

In light of the results of this study, our data strongly support the hypothesis that TatA, TatB, and TatC generate locally destabilized membranes that permit the membrane passage of folded proteins (25, 60). The "membrane weakening and pulling" hypothesis proposed that this process could depend on membrane destabilization by multiple aligned TatA TMHs (60), which was later supported by an experimental demonstration of membrane destabilization, MD simulations, and recently by electrochromic shift measurements (8, 25, 59). A conformational switch of the TatA APH in response to substrate binding has been first demonstrated in thylakoids and then in the *E. coli* system and has been suggested to contribute to this membrane destabilization (25, 26).

Hydrophobic mismatches are not only generated by the TMHs of TatA and TatB, but also by the short TMHs 5 and 6 of TatC. Notably, the TMHs of TatA and TatB are both shown to interact with these two TatC helices in a resting state (24, 28, 36), which is likely the reason for the shown importance of the specific short length of the TatB TMH for stable TatBC associations (Fig. 4). As substrate binding has been shown to trigger the association of TatA (20–22, 61), as TatA association has been reported to precede the translocation of TatBC-bound Tat substrates (18, 19), as substrate has been shown to trigger membrane permeabilization by TatA *in vitro* (25), and as TatA assemblies have the capacity to destabilize the membrane (Fig. 8), we would like to suggest that larger TatA assemblies may form at TatABC complexes to enable Tat transport (see Fig. 12). In principle, such an interaction would explain why most TatA is lost during purification of TatBC complexes (15), and this model also explains how a simple conformational shift of TatC helices 5 and 6 in response to substrate binding may enhance the hydrophobic mismatch at the TatBC core to induce the binding of a large number of TatA protomers to the translocation site, which induces membrane destabilization where it is needed (Fig. 12).

The model also gives an idea about the region of membrane destabilization, which is essentially the region underneath the APHs. There are two plausible pathways through the destabilized membrane: (1) the two staggered rows of TatA, which are vis-à-vis positioned in the cluster, could open and permit the passage of the Tat substrate or (2) the TMHs remain in the center of the association and the substrate passes through the thinnest point of the destabilized membrane close to the center of the TatA cluster. As Tat substrates can be large in

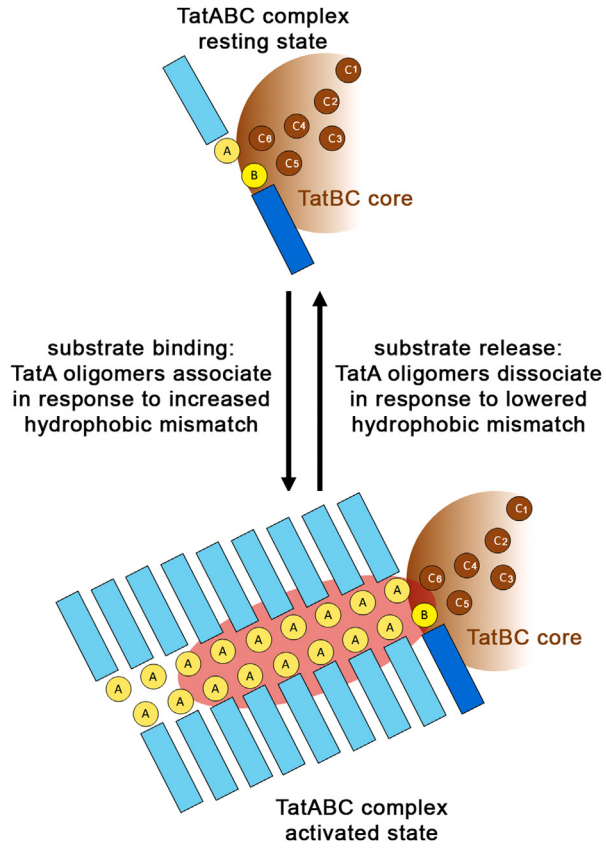

Figure 12. Potential substrate-induced assembly of membrane-weakening TatA-clusters at TatBC core complexes. Top view on the cytoplasmic face of the membrane, only positions of TMHs and APHs are schematically depicted. TMHs of TatA, TatB, and TatC are labeled A, B, or C, respectively. In case of TatC, which has six TMHs, the helix number is also indicated. The destabilized membrane region is highlighted by a *reddish* background. Only one docking site for TatA at the oligomeric TatBC core complex is exemplified in the scheme. The substrate that induces the conformational switch is only mentioned but not shown for clarity reasons. The color code for the TMHs and APHs is taken from Figure 1. See text for details.

diameter, it is likely that both happen as follows: TMHs may lose their contact and APHs may dissociate to permit the passage of globular proteins. In such a situation of disorder, it could well be that TatA exchanges with TatB at its TatC-binding site, especially when the system is saturated with transported substrates (28). It is also possible that an opening of TatBC complexes can contribute to the TatA recruitment, such as proposed previously (2, 24, 36). Our simulations show that TatA can form stable clusters with two interacting rows of TMHs in the center. From the energetic point of view, MD simulations indicate that there will not be any stable ring-shaped TatA assembly with an aqueous hole (8). Instead, the hydrophobic mismatch can be expected to trigger associations of the TMHs, which preferentially should be linear to accommodate aligned APHs at the membrane surface that contribute to membrane destabilization (Figs. 8 and 9). During the passage, transient aqueous holes would be formed that would cause uncontrolled proton flux for a very short time span. Such a proton leakage would agree with the finding that about 80,000 protons pass through the membrane per

transported protein (62), albeit proton flux does not energize the transport (63, 64). The membrane-thinning assemblies of TatA are expected to alter the diffusion rate in the membrane, and this has been observed in a recent study that is currently published as preprint in BioRxiv (65). Although it is clear from many studies that the electric potential is required at certain steps of the pathway, one of which may be the proposed conformational transition of the TatBC core complex that induces the recruitment of TatA (which is PMF-dependent; (20, 21)), the driving force for the transport remains to be clarified. In principle, it would be possible that the transmembrane signal peptide insertion as catalyzed by TatBC complexes (30) constitutes this driving force, as the signal peptide remains bound to the TatBC complex during transport of the mature domain (66). Future experiments surely will shed further light on this highly fascinating transport system.

Experimental procedures

Bacterial strains and growth conditions

The *E. coli* Δ*tatABCD* Δ*tatE* strain DADE (40), and its parental strain MC4100 (67), were used for localization and complementation studies. *E. coli* XL1-Blue Mrf' Kan (Stratagene) or *E. coli* DH5α λ *pir*$^+$ were used for cloning. Unless otherwise stated, bacteria were grown aerobically at 37 °C on LB medium (1% (w/v) tryptone, 1% (w/v) NaCl, 0.5% (w/v) yeast extract) in the presence of the appropriate antibiotics (25 μg/ml chloramphenicol, 100 μg/ml ampicillin, 12.5 μg/ml tetracycline, 15 μg/ml kanamycin). For subcellular fractionations, all cultures were normalized to an OD_{600} of 1.0. For growth curves, the OD_{600} was measured with technical triplicates in 15-min intervals with cultures grown at 37 °C in shaking 96-well plates (culture volume: 200 μl), using the SpectraMax iD3 Microplate Reader (Molecular Devices).

Genetic methods and plasmids

For analyses of Tat functionality and for optimization of the MT3–gold-labeling method, the TatABC components were constitutively overproduced using the natural P_{tatA} promoter and *tatABC* operon organization in plasmid pABS-*tatABC* and derivatives thereof (39). The shortenings and extensions of the hydrophobic helices in TatA and TatB were carried out by QuikChange mutagenesis. Primers are listed in Table 1.

To analyze MT3–gold-labeled Tat components at WT level, the *tatABC* operon and its derivatives were cloned into pAH120-Ptat-*tatABC*-strep (see primer table), which is a *tatABC*-containing derivative of pAH120-Ptat-*tatA*-strep-ΔBamHI (68). Briefly, the MT3-tag (including the linker) was amplified from the pMAL-c2x-MT3 (48) using primers MT-l-F and MT-R, cut with BglII/BssHII, and ligated into the backbone of the plasmid pAH120-Ptat-*tatABC*-strep cut with BamHI/BssHII. This resulted in pAH120-Ptat-*tatABC*-MT3, which was then cut with NdeI/BamHI and ligated into the corresponding sites of pABS-*tatABC*-H6 (27), resulting in pABS-*tatABC*-MT3. To construct pABS-*tatA*-MT3, *tatA* was amplified from pABS-*tatABC*-MT3 using primers pABS-*tatA*-MT3-R and pABS-*tatABC*-SalI-F, and the fragment was cut with SalI/SacI and ligated into the plasmid backbone obtained by restriction of pABS-*tatABC*-H6 with the same enzymes. The same procedure was followed to construct pABS-*tatAB*-MT3, except that the primers utilized were pABS-*tatB*-MT3-R and pABS-*tatABC*-SalI-F. To append the *tatBC*-genes to the *tatA*-MT3-construct, these were amplified from the pABS-Ptat-*tatABC*-MT3 plasmid using primers pABS-*tatB*-BamHI-F and pABS-*tatC*-ClaI-R, and the fragment was cut with BamHI/ClaI and ligated into the respective sites of the pABS-Ptat-*tatA*-MT3 backbone. The same steps were taken to construct the pABS-*tatAB*-MT3-*tatC* plasmid, only that primers pABS-*tatC*-F and pABS-*tatC*-ClaI-R were used and the fragment was ligated into the backbone of pABS-Ptat-*tatAB*-MT3. Finally, both the *tatA*-MT3-BC and *tatAB*-MT3-*tatC* constructs were transferred back into pAH120 by restriction of pAH120-Ptat-*tatABC*-MT3, pABS-*tatA*-MT3-*tatBC*, and pABS-*tatAB*-MT3-*tatC* with NdeI/XbaI and ligation of the *tat*-fragments into the pAH120-backbone. Vectors were integrated into the chromosomal lambda attachment site according to the protocol of Haldiman and Wanner (69). pRK-*hip* was used for constitutive low-level expression of the *hip* gene from its own promotor (42).

Biochemical methods

Subcellular fractionations into periplasm, membranes, and cytoplasm were performed with 50 ml cultures as described previously (68). SDS-PAGE analysis was carried out by standard methods (70). BN-PAGE was performed as described previously (32), but without β-mercaptoethanol in the buffers. TatABC complexes were solubilized with 1% digitonin. For immunoblots, proteins were semi-dry blotted on nitrocellulose membranes, and blots were developed using antibodies directed against synthetic C-terminal peptides of TatA, TatB, TatC, or polyclonal rabbit serum against purified HiPIP or PspA, using the ECL system (GE Healthcare) for signal detection. DsbA antibody was obtained from Enogene Biotech (New York). YidC antibody was a gift of Andreas Kuhn (Hohenheim). Horseradish peroxidase–conjugated goat anti rabbit or goat anti mouse antibodies (Roth) served as secondary antibodies. Biotin carboxyl carrier protein was detected by horseradish peroxidase–coupled Strep-Tactin (IBA). The chain formation phenotype was assessed by phase contrast microscopy. SDS sensitivity was determined by aerobic growth in LB medium containing 4% (w/v) SDS, using the quotient of the OD_{600} with/without SDS after 3 h of growth (41). For carbonate washes of membranes, samples were treated as described before (25).

Electron microscopy – sample preparation

Bacterial cells (20 ml culture, 5% inoculum) were grown at 37 °C at 140 rpm to OD_{600} ~0.5, then 0.4 ml of an aqueous 25 mM tetrachloroauric acid solution were added, and growth was continued for 90 min at 37 °C and 120 rpm. Cells were sedimented (10 min, 3820*g*, 4 °C), resuspended in 1.5 ml 100 mM Hepes pH 7.0, 90 mM sucrose (buffer A), and incubated for 5 min at room temperature (RT). Cells were sedimented again (2 min, RT, 6800*g*) and the incubation/

Table 1
Primers used in this study[a]

Mutagenesis primers[b,c]	Sequence (5′>3′)
Deletions	
tatA-1-F	CAGTATTTGGCAGTTAATTATTGCCGTCATCG
tatA-3-F	GTATTTGGCAGTTAGCCGTCATCGTTG
tatA-5-F	GGTATCAGTATTTGGCAGTTAATCGTTGTACTGCTTTTTGGC
tatA-7-F	CAGTATTTGGCAGTTAGTACTGCTTTTTGGC
tatB-1-F	CGGTTTTAGCGAACTGTTGGTGTTCATCATC
tatB-3-F	GTTTTAGCGAACTGTTCATCATCGGCC
Leucine insertions	
tatA+1-F	CAGTATTTGGCAGTTATTGCTTATTATTGCCGTCATCGTTG
tatA+2-F	CAGTATTTGGCAGTTATTGCTTCTCATTATTGCCGTCATCGTTG
tatA+3-F	GGCAGTTATTGCTTCTCTTAATTATTGCCGTCATCG
tatA+4-F	GGCAGTTATTGCTTCTCTTATTGATTATTGCCGTCATCG
tatA+5-F	GTTATTGCTTCTCTTATTGCTTATTATTGCCGTCATCGTTG
tatA+6-F	GTTATTGCTTCTCTTATTGCTTCTCATTATTGCCGTCATCGTTG
tatA+7-F	GCTTCTCTTATTGCTTCTCTTAATTATTGCCGTCATCGTTG
tatB+3-F	CGGTTTTAGCGAACTGCTGCTCCTTCTATTGGTGTTCATCATC
tatB+4-F	CGGTTTTAGCGAACTGCTGCTCCTTCTGCTATTGGTGTTCATCATC
Fusion Primers	
MT-l-F	CGACCGGGATCCAATTCGAGCTCGAACAACAACAAC
MT-R	TTATCGGCGCGCTTGTAAAACGACGGCCAGTGC
pABS-*tatB*-BamHI-F	CCCGAGGGATCCGATAAAGAGCAGGTGTAATCC
pABS-*tatC*-ClaI-R	GGCCGTATCGATCTATTCTTCAGTTTTTTCGCTTTCTGCTTC
pABS-*tatA*-MT3-R	GTTGTTGTTGTTCGAGCTCGAATTAGATCCCACCTGCTCTTTATCGTGGCGCTTCG
pABS-*tatABC*-SalI-F	AGGGCATCGGTCGACGCTCTCC
pABS-*tatB*-MT3	GTTGTTGTTGTTCGAGCTCGAATTAGATCCCGGTTTATCACTCGACGAAGGGGAAG
pABS-*tatC*-F	CCGAGCGGATCCTCGTCGAGTGATAAACCGTAAAC
Primers for cloning of pAH120-Ptat-*tatABC*-strep	
tatA-NdeI-F	GAACACATATGGGTGGTATCAGTATTTGGC
tatC-BamHI-R	AAGGATCCTTCTTCAGTTTTTTCGCTTTCTGC

[a] Primer sequences are given in 5′-3′ direction.
[b] Corresponding reverse primers covered the same sequence.
[c] Templates for larger deletions or insertions were the constructs with smaller deletions or insertions.

resuspension was repeated. Cells were then resuspended in 1 ml buffer A containing 2.5% glutaraldehyde, incubated for > 20 min at RT, washed with 1 ml buffer A, sedimented (2 min, 6177*g*, RT), and washed twice in 100 mM Hepes pH 6.9, 90 mM sucrose, 10 mM $MgCl_2$, 10 mM $CaCl_2$, sedimented again, and embedded either in SPURR epoxy resin (71) or in LR-White resin (72). Seventy nanometer ultrathin sections were cut using an ultramicrotome with a diamond knife (Ultracut; Leica Biosystems) and picked up with neoprene-coated Cu-grids (300 mesh, hexagonal). *TEM image registration and processing:* Unstained samples were analyzed in the elastic bright-field mode with an in-column energy-filter transmission electron microscope (Libra 120 plus, Zeiss). The energy-selecting slit aperture was set to 15 eV energy width, and images were recorded with a cooled bottom-mount 2 × 2 k CCD (SharpEye, Tröndle) at nominal magnifications from ×12,500 to × 50,000 near Gaussian or at 500 to 1500 nm underfocus. Data acquisition and spectrum/image-analysis were done using the iTEM software package (Olympus Soft Imaging Solutions Ltd). Images were further processed with the Corel Draw Graphics Suite X7 (Corel Ltd) and ImageJ Fiji software (https://fiji.sc/) (73). *PEELS:* PEELS was done with unstained 35 nm ultrathin sections of epoxy resin-embedded *E. coli* strain DADE/pABS- *tatAB(MT3)*-C with MT3-gold as the only electron-dense intracellular material. PEELS registration was performed in the energy range from 30 to 139 eV, specific for the Au-O_{23} edge, with a 100 μm spectrum entrance aperture and five acquisition cycles pro record. Spectrum magnification was set to 200-fold, and the illumination aperture to 0.16 mrad with 4 μA emission current; exposure time: 0.2 s, nominal magnification: ×31,500. *Electron spectroscopic element mapping*: Data acquisition was performed on well-defined Au-MT3 clusters and the energy-selective slit was set to 8 eV width. Jump-ratio images were registered at 66 eV (=Emax) and 38 eV (=first window). These energy settings were taken from PEEL spectrum data of the MT3-gold assemblies of interest. Exposure time: 2 s, illumination aperture: 0.63 mrad, nominal magnification: ×31,500.

MD simulation

MD simulations were performed using the GROMACS simulation package, version 2019.5 (74). The MARTINI v2.1 coarse-grained force field (75–77) was applied to simulate lipids, peptides, and solvent. In all simulations, the system was coupled to a constant temperature bath by v-rescale algorithm (78) with a relaxation time of 1.0 ps. Simulations were performed at 320 K. Periodic boundary conditions were applied to simulate bulk behavior. The time step used in the simulation was 20 fs. The dielectric constant in the simulations was ε_r = 15. The pressure was coupled to 1 bar employing the Parrinello-Rahman barostat (79) with a relaxation time of 12.0 ps. Unless stated otherwise, the TatA membrane system consisted of 22 TatA proteins in a lipid bilayer with 75% phosphatidylethanolamine, 19% phosphatidylglycerol, and 6% cardiolipin, which is a usual ratio of these lipids in the cytoplasmic membrane of *E. coli* (80). For the MD simulations of TatA associations, a coarse-grained TatA model up to residue Glu47 was constructed based on the known NMR structure (PDB 2MN7, 10). To model the linear assembly of TatA proteins observed in the TEM experiments, 22 copies of the equilibrated TatA structure were placed vis-à-vis in two rows of 11 subunits and inserted in the membrane *via* deletion of all overlapping membrane lipids. The overall dimension of these 22-mers, about 20 nm in length, closely match to the ones observed in METTEM. This system was then equilibrated for 500 ns to enable adaption of the membrane. The TMHs readily associated in a staggered way with all TatA proteins included in the linear complex. For all simulations, the TatA sequences up to position Lys49 were used, as C-terminal truncation analyses have shown that a TatA of exactly that length is still functional (12). MODELLER 9.24 (81) was used to create the TatA variants. The resulting data were evaluated by MDAnalysis 0.20.1 (82). The lipid tail order parameter S_{zz} = ½

($3(\mathbf{b}^*\mathbf{n})^2-1$) was determined to quantify the average orientation of tail bond vectors **b** with respect to the bilayer normal **n** (83). Order parameter time series were checked for equilibration and decorrelated using the pymbar package (84–86). Angles between the TMH and the APH were calculated between two vectors connecting the center of masses (COMs) of residues Gly21, Thr22, and Lys23 for the hinge either with the COM of residues Ala13, Val14, and Ile15 for the TMH or with the COM of residues Ile28, Gly29, and Ser30 for the APH (WT numbering). Images of the simulations were generated using NGLview v2.7.7 (87).

Data availability

All data are contained within the article.

Supporting information—This article contains supporting information.

Acknowledgments—We thank Sybille Traupe and Katrin Gunka (LUH, Hannover) for excellent technical assistance. We gratefully acknowledge the skillful work and experience in electron microscopic sample preparation by Inge Kristen, Sabine Schmidt, and Ina Schleicher (HZI, Braunschweig).

Author contributions—D. M.-B. and K. S. S. formal analysis; D. M.-B., M. T. R., D. A. T., and H. L. investigation; D. M.-B., M. T. R., H. L., and H. J. R. methodology; D. M.-B., K. S. S., H. L., and T. B. visualization; D. M.-B., M. T. R., D. A. T., L. J. E., K. S. S., H. L., H. J. R., and T. B. writing–review and editing; L. J. E., K. S. S., H. J. R., and T. B. supervision; L. J. E. and K. S. S. validation; T. B. conceptualization; T. B. funding acquisition; T. B. writing–original draft.

Funding and additional information—This study was supported by the DFG grant BR 2285/8-1 to T. B.

Conflict of interest—The authors declare that they have no conflicts of interest with the contents of this article.

Abbreviations—The abbreviations used are: APH, amphipathic helix; BN-PAGE, Blue-Native Polyacrylamide Gel Electrophoresis; COM, center of mass; METTEM, metal-tagging transmission electron microscopy; PEELS, Parallel Electron Energy-Loss Spectroscopy; Tat, twin-arginine translocation; TMH, transmembrane helix.

References

1. Hou, B., and Brüser, T. (2011) The Tat-dependent protein translocation pathway. *Biomol. Concepts* **2**, 507–523
2. Cline, K. (2015) Mechanistic aspects of folded protein transport by the twin arginine translocase (tat). *J. Biol. Chem.* **290**, 16530–16538
3. Petrů, M., Wideman, J., Moore, K., Alcock, F., Palmer, T., and Doležal, P. (2018) Evolution of mitochondrial TAT translocases illustrates the loss of bacterial protein transport machines in mitochondria. *BMC Biol.* **16**, 141
4. Jongbloed, J. D., Grieger, U., Antelmann, H., Hecker, M., Nijland, R., Bron, S., *et al.* (2004) Two minimal Tat translocases in *Bacillus*. *Mol. Microbiol.* **54**, 1319–1325
5. Müller, M., and Klösgen, R. B. (2005) The Tat pathway in bacteria and chloroplasts. *Mol. Membr. Biol.* **22**, 113–121
6. Yen, M.-R., Tseng, Y.-H., Nguyen, E. H., Wu, L.-F., and Saier, M. H. (2002) Sequence and phylogenetic analyses of the twin-arginine targeting (Tat) protein export system. *Arch. Microbiol.* **177**, 441–450
7. Hu, Y., Zhao, E., Li, H., Xia, B., and Jin, C. (2010) Solution NMR structure of the TatA component of the twin-arginine protein transport system from gram-positive bacterium *Bacillus subtilis*. *J. Am. Chem. Soc.* **132**, 15942–15944
8. Rodriguez, F., Rouse, S. L., Tait, C. E., Harmer, J., de Riso, A., Timmel, C. R., *et al.* (2013) Structural model for the protein-translocating element of the twin-arginine transport system. *Proc. Natl. Acad. Sci. U. S. A.* **110**, E1092–E1101
9. Zhang, Y., Wang, L., Hu, Y., and Jin, C. (2014) Solution structure of the TatB component of the twin-arginine translocation system. *Biochim. Biophys. Acta* **1838**, 1881–1888
10. Zhang, Y., Hu, Y., Li, H., and Jin, C. (2014) Structural basis for TatA oligomerization: an NMR study of *Escherichia coli* TatA dimeric structure. *PLoS One* **9**, e103157
11. Warren, G., Oates, J., Robinson, C., and Dixon, A. M. (2009) Contributions of the transmembrane domain and a key acidic motif to assembly and function of the TatA complex. *J. Mol. Biol.* **388**, 122–132
12. Lee, P. A., Buchanan, G., Stanley, N. R., Berks, B. C., and Palmer, T. (2002) Truncation analysis of TatA and TatB defines the minimal functional units required for protein translocation. *J. Bacteriol.* **184**, 5871–5879
13. Rollauer, S. E., Tarry, M. J., Graham, J. E., Jaaskelainen, M., Jager, F., Johnson, S., *et al.* (2012) Structure of the TatC core of the twin-arginine protein transport system. *Nature* **492**, 210–214
14. Behrendt, J., Standar, K., Lindenstrauss, U., and Brüser, T. (2004) Topological studies on the twin-arginine translocase component TatC. *FEMS Microbiol. Lett.* **234**, 303–308
15. Behrendt, J., and Brüser, T. (2014) The TatBC complex of the Tat protein translocase in *Escherichia coli* and its transition to the substrate-bound TatABC complex. *Biochemistry* **53**, 2344–2354
16. Bolhuis, A., Mathers, J. E., Thomas, J. D., Barrett, C. M., and Robinson, C. (2001) TatB and TatC form a functional and structural unit of the twin-arginine translocase from *Escherichia coli*. *J. Biol. Chem.* **276**, 20213–20219
17. Behrendt, J., Lindenstrauss, U., and Brüser, T. (2007) The TatBC complex formation suppresses a modular TatB-multimerization in *Escherichia coli*. *FEBS Lett.* **581**, 4085–4090
18. Cline, K., and Mori, H. (2001) Thylakoid ΔpH-dependent precursor proteins bind to a cpTatC-Hcf106 complex before Tha4-dependent transport. *J. Cell Biol.* **154**, 719–729
19. Mori, H., and Cline, K. (2002) A twin arginine signal peptide and the pH gradient trigger reversible assembly of the thylakoid ΔpH/Tat translocase. *J. Cell Biol.* **157**, 205–210
20. Rose, P., Fröbel, J., Graumann, P. L., and Müller, M. (2013) Substrate-dependent assembly of the Tat translocase as observed in live *Escherichia coli* cells. *PLoS One* **8**, e69488
21. Alcock, F., Baker, M. A. B., Greene, N. P., Palmer, T., Wallace, M. I., and Berks, B. C. (2013) Live cell imaging shows reversible assembly of the TatA component of the twin-arginine protein transport system. *Proc. Natl. Acad. Sci. U. S. A.* **110**, E3650–E3659
22. Dabney-Smith, C., and Cline, K. (2009) Clustering of C-terminal stromal domains of Tha4 homo-oligomers during translocation by the tat protein transport system. *Mol. Biol. Cell* **20**, 2060–2069
23. Leake, M. C., Greene, N. P., Godun, R. M., Granjon, T., Buchanan, G., Chen, S., *et al.* (2008) Variable stoichiometry of the TatA component of the twin-arginine protein transport system observed by *in vivo* single-molecule imaging. *Proc. Natl. Acad. Sci. U. S. A.* **105**, 15376–15381
24. Aldridge, C., Ma, X., Gerard, F., and Cline, K. (2014) Substrate-gated docking of pore subunit Tha4 in the TatC cavity initiates Tat translocase assembly. *J. Cell Biol.* **205**, 51–65
25. Hou, B., Heidrich, E. S., Mehner-Breitfeld, D., and Brüser, T. (2018) The TatA component of the twin-arginine translocation system locally weakens the cytoplasmic membrane of *Escherichia coli* upon protein substrate binding. *J. Biol. Chem.* **293**, 7592–7605
26. Aldridge, C., Storm, A., Cline, K., and Dabney-Smith, C. (2012) The chloroplast twin arginine transport (Tat) component, Tha4, undergoes conformational changes leading to Tat protein transport. *J. Biol. Chem.* **287**, 34752–34763
27. Geise, H., Heidrich, E. S., Nikolin, C. S., Mehner-Breitfeld, D., and Brüser, T. (2019) A potential late stage intermediate of twin-arginine

dependent protein translocation in *Escherichia coli*. *Front. Microbiol.* **10**, 1482
28. Habersetzer, J., Moore, K., Cherry, J., Buchanan, G., Stansfeld, P. J., and Palmer, T. (2017) Substrate-triggered position switching of TatA and TatB during tat transport in *Escherichia coli*. *Open Biol.* **7**, 170091
29. Berks, B. C. (1996) A common export pathway for proteins binding complex redox cofactors. *Mol. Microbiol.* **22**, 393–404
30. Fröbel, J., Rose, P., Lausberg, F., Blümmel, A.-S., Freudl, R., and Müller, M. (2012) Transmembrane insertion of twin-arginine signal peptides is driven by TatC and regulated by TatB. *Nat. Commun.* **3**, 1311
31. Oates, J., Barrett, C. M. L., Barnett, J. P., Byrne, K. G., Bolhuis, A., and Robinson, C. (2005) The *Escherichia coli* twin-arginine translocation apparatus incorporates a distinct form of TatABC complex, spectrum of modular TatA complexes and minor TatAB complex. *J. Mol. Biol.* **346**, 295–305
32. Richter, S., and Brüser, T. (2005) Targeting of unfolded PhoA to the TAT translocon of *Escherichia coli*. *J. Biol. Chem.* **280**, 42723–42730
33. Gohlke, U., Pullan, L., McDevitt, C. A., Porcelli, I., de Leeuw, E., Palmer, T., *et al.* (2005) The TatA component of the twin-arginine protein transport system forms channel complexes of variable diameter. *Proc. Natl. Acad. Sci. U. S. A.* **102**, 10482–10486
34. Pettersson, P., Patrick, J., Jakob, M., Jacobs, M., Klösgen, R. B., Wennmalm, S., *et al.* (2021) Soluble TatA forms oligomers that interact with membranes: structure and insertion studies of a versatile protein transporter. *Biochim. Biophys. Acta* **1863**, 183529
35. White, G. F., Schermann, S. M., Bradley, J., Roberts, A., Greene, N. P., Berks, B. C., *et al.* (2010) Subunit organization in the TatA complex of the twin arginine protein translocase. a site-directed EPR spin labeling study. *J. Biol. Chem.* **285**, 2294–2301
36. Alcock, F., Stansfeld, P. J., Basit, H., Habersetzer, J., Baker, M. A., Palmer, T., *et al.* (2016) Assembling the Tat protein translocase. *Elife* **5**, e20718
37. Baeza-Delgado, C., Marti-Renom, M. A., and Mingarro, I. (2013) Structure-based statistical analysis of transmembrane helices. *Eur. Biophys. J.* **42**, 199–207
38. Holt, A., and Killian, J. A. (2010) Orientation and dynamics of transmembrane peptides: the power of simple models. *Eur. Biophys. J.* **39**, 609–621
39. Berthelmann, F., and Brüser, T. (2004) Localization of the Tat translocon components in *Escherichia coli*. *FEBS Lett.* **569**, 82–88
40. Wexler, M., Sargent, F., Jack, R. L., Stanley, N. R., Bogsch, E. G., Robinson, C., *et al.* (2000) TatD is a cytoplasmic protein with DNase activity. No requirement for TatD family proteins in sec-independent protein export. *J. Biol. Chem.* **275**, 16717–16722
41. Ize, B., Stanley, N. R., Buchanan, G., and Palmer, T. (2003) Role of the *Escherichia coli* Tat pathway in outer membrane integrity. *Mol. Microbiol.* **48**, 1183–1193
42. Brüser, T., Yano, T., Brune, D. C., and Daldal, F. (2003) Membrane targeting of a folded and cofactor-containing protein. *Eur. J. Biochem.* **270**, 1211–1221
43. Mercogliano, C. P., and DeRosier, D. J. (2006) Gold nanocluster formation using metallothionein: mass spectrometry and electron microscopy. *J. Mol. Biol.* **355**, 211–223
44. Bouchet-Marquis, C., Pagratis, M., Kirmse, R., and Hoenger, A. (2012) Metallothionein as a clonable high-density marker for cryo-electron microscopy. *J. Struct. Biol.* **177**, 119–127
45. Nishino, Y., Yasunaga, T., and Miyazawa, A. (2007) A genetically encoded metallothionein tag enabling efficient protein detection by electron microscopy. *J. Electron. Microsc. (Tokyo)* **56**, 93–101
46. Morphew, M. K., O'Toole, E. T., Page, C. L., Pagratis, M., Meehl, J., Giddings, T., *et al.* (2015) Metallothionein as a clonable tag for protein localization by electron microscopy of cells. *J. Microsc.* **260**, 20–29
47. Mercogliano, C. P., and DeRosier, D. J. (2007) Concatenated metallothionein as a clonable gold label for electron microscopy. *J. Struct. Biol.* **160**, 70–82
48. Diestra, E., Fontana, J., Guichard, P., Marco, S., and Risco, C. (2009) Visualization of proteins in intact cells with a clonable tag for electron microscopy. *J. Struct. Biol.* **165**, 157–168
49. Jack, R. L., Sargent, F., Berks, B. C., Sawers, G., and Palmer, T. (2001) Constitutive expression of *Escherichia coli tat* genes indicates an important role for the twin-arginine translocase during aerobic and anaerobic growth. *J. Bacteriol.* **183**, 1801–1804
50. Berthelmann, F., Mehner, D., Richter, S., Lindenstrauss, U., Lünsdorf, H., Hause, G., *et al.* (2008) Recombinant expression of *tatABC* and *tatAC* results in the formation of interacting cytoplasmic TatA tubes in *Escherichia coli*. *J. Biol. Chem.* **283**, 25281–25289
51. Walther, T. H., Grage, S. L., Roth, N., and Ulrich, A. S. (2010) Membrane alignment of the pore-forming component TatA(d) of the twin-arginine translocase from *Bacillus subtilis* resolved by solid-state NMR spectroscopy. *J. Am. Chem. Soc.* **132**, 15945–15956
52. Kobayashi, R., Suzuki, T., and Yoshida, M. (2007) *Escherichia coli* phage-shock protein A (PspA) binds to membrane phospholipids and repairs proton leakage of the damaged membranes. *Mol. Microbiol.* **66**, 100–109
53. Mehner, D., Osadnik, H., Lunsdorf, H., and Brüser, T. (2012) The Tat system for membrane translocation of folded proteins recruits the membrane-stabilizing Psp machinery in *Escherichia coli*. *J. Biol. Chem.* **287**, 27834–27842
54. Bernal-Cabas, M., Miethke, M., Antelo-Varela, M., Aguilar Suárez, R., Neef, J., Schön, L., *et al.* (2020) Functional association of the stress-responsive LiaH protein and the minimal TatAyCy protein translocase in *Bacillus subtilis*. *Biochim. Biophys. Acta Mol. Cell Res.* **1867**, 118719
55. Katsuta, H., Sawada, Y., and Sokabe, M. (2019) Biophysical mechanisms of membrane-thickness-dependent MscL gating: an all-atom molecular dynamics study. *Langmuir* **35**, 7432–7442
56. Jensen, M.Ø., and Mouritsen, O. G. (2004) Lipids do influence protein function-the hydrophobic matching hypothesis revisited. *Biochim. Biophys. Acta* **1666**, 205–226
57. Windisch, D., Ziegler, C., Grage, S. L., Bürck, J., Zeitler, M., Gor'kov, P. L., *et al.* (2015) Hydrophobic mismatch drives the interaction of E5 with the transmembrane segment of PDGF Receptor. *Biophys. J.* **109**, 737–749
58. Garlick, E., Thomas, S. G., and Owen, D. M. (2021) Super-resolution imaging approaches for quantifying F-actin in immune cells. *Front. Cell Dev. Biol.* **9**, 676066
59. Asher, A. H., and Theg, S. M. (2021) Electrochromic shift supports the membrane destabilization model of Tat-mediated transport and shows ion leakage during Sec transport. *Proc. Natl. Acad. Sci. U. S. A.* **118**, e2018122118
60. Brüser, T., and Sanders, C. (2003) An alternative model of the twin arginine translocation system. *Microbiol. Res.* **158**, 7–17
61. Dabney-Smith, C., Mori, H., and Cline, K. (2006) Oligomers of Tha4 organize at the thylakoid Tat translocase during protein transport. *J. Biol. Chem.* **281**, 5476–5483
62. Alder, N. N., and Theg, S. M. (2003) Energetics of protein transport across biological membranes. a study of the thylakoid ΔpH-dependent/cpTat pathway. *Cell* **112**, 231–242
63. Braun, N. A., Davis, A. W., and Theg, S. M. (2007) The chloroplast Tat pathway utilizes the transmembrane electric potential as an energy source. *Biophys. J.* **93**, 1993–1998
64. Bageshwar, U. K., and Musser, S. M. (2007) Two electrical potential-dependent steps are required for transport by the *Escherichia coli* Tat machinery. *J. Cell Biol.* **179**, 87–99
65. [preprint] Varadarajan, A., Oswald, F., Lill, H., Peterman, E. J., and Bollen, Y. J. M. (2020) Rapid diffusion of large TatA complexes detected using single particle tracking microscopy. *BioRxiv*. https://doi.org/10.1101/2020.05.14.095463
66. Gerard, F., and Cline, K. (2006) Efficient twin arginine translocation (Tat) Pathway transport of a precursor protein covalently anchored to its initial cpTatC binding site. *J. Biol. Chem.* **281**, 6130–6135
67. Casadaban, M. J. (1976) Transposition and fusion of the lac genes to selected promoters in *Escherichia coli* using bacteriophage lambda and Mu. *J. Mol. Biol.* **104**, 541–555
68. Taubert, J., Hou, B., Risselada, H. J., Mehner, D., Lünsdorf, H., Grubmüller, H., *et al.* (2015) TatBC-independent TatA/Tat substrate interactions contribute to transport efficiency. *PLoS One* **10**, e0119761
69. Haldimann, A., and Wanner, B. L. (2001) Conditional-replication, integration, excision, and retrieval plasmid-host systems for gene structure-function studies of bacteria. *J. Bacteriol.* **183**, 6384–6393

70. Laemmli, U. K. (1970) Cleavage of structural proteins during the assembly of the head of bacteriophage T4. *Nature* **227**, 680–685
71. Lünsdorf, H., Strömpl, C., Osborn, A. M., Bennasar, A., Moore, E. R., Abraham, W. R., *et al.* (2001) Approach to analyze interactions of microorganisms, hydrophobic substrates, and soil colloids leading to formation of composite biofilms, and to study initial events in microbiogeological processes. *Met. Enzymol.* **336**, 317–331
72. Fernández de Castro, I., Fernández, J. J., Barajas, D., Nagy, P. D., and Risco, C. (2017) Three-dimensional imaging of the intracellular assembly of a functional viral RNA replicase complex. *J. Cell Sci.* **130**, 260–268
73. Schindelin, J., Arganda-Carreras, I., Frise, E., Kaynig, V., Longair, M., Pietzsch, T., *et al.* (2012) Fiji: an open-source platform for biological-image analysis. *Nat. Met.* **9**, 676–682
74. Lindahl, E., Abraham, M. J., Hess, B., and van der Spoel, D. (2019) GROMACS 2019.5 source code. *Zenodo*. https://doi.org/10.5281/zenodo.3577986
75. Marrink, S. J., de Vries, A. H., and Mark, A. E. (2004) Coarse grained model for semiquantitative lipid simulations. *J. Phys. Chem. B* **108**, 750–760
76. Marrink, S. J., Risselada, H. J., Yefimov, S., Tieleman, D. P., and de Vries, A. H. (2007) The MARTINI force field: Coarse grained model for biomolecular simulations. *J. Phys. Chem. B* **111**, 7812–7824
77. Monticelli, L., Kandasamy, S. K., Periole, X., Larson, R. G., Tieleman, D. P., and Marrink, S. J. (2008) The MARTINI coarse-grained force field: extension to proteins. *J. Chem. Theor. Comput.* **4**, 819–834
78. Bussi, G., Donadio, D., and Parrinello, M. (2007) Canonical sampling through velocity rescaling. *J. Chem. Phys.* **126**, 14101
79. Parrinello, M., and Rahman, A. (1981) Polymorphic transitions in single crystals: a new molecular dynamics method. *J. Appl. Phys.* **52**, 7182–7190
80. Raetz, C. R. (1978) Enzymology, genetics, and regulation of membrane phospholipid synthesis in *Escherichia coli*. *Microbiol. Rev.* **42**, 614–659
81. Webb, B., and Sali, A. (2016) Comparative protein structure modeling using MODELLER. *Curr. Protoc. Protein Sci.* **86**, 2.9.1–2.9.37
82. Michaud-Agrawal, N., Denning, E. J., Woolf, T. B., and Beckstein, O. (2011) MDAnalysis: a toolkit for the analysis of molecular dynamics simulations. *J. Comput. Chem.* **32**, 2319–2327
83. MacDermaid, C. M., Kashyap, H. K., DeVane, R. H., Shinoda, W., Klauda, J. B., *et al.* (2015) Molecular dynamics simulations of cholesterol-rich membranes using a coarse-grained force field for cyclic alkanes. *J. Chem. Phys.* **143**, 243144
84. Chodera, J. D., Swope, W. C., Pitera, J. W., Seok, C., and Dill, K. A. (2007) Use of the weighted histogram analysis method for the analysis of simulated and parallel tempering simulations. *J. Chem. Theor. Comput.* **3**, 26–41
85. Shirts, M. R., and Chodera, J. D. (2008) Statistically optimal analysis of samples from multiple equilibrium states. *J. Chem. Phys.* **129**, 124105
86. Chodera, J. D. (2016) A simple method for automated equilibration detection in molecular simulations. *J. Chem. Theor. Comput.* **12**, 1799–1805
87. Nguyen, H., Case, D. A., and Rose, A. S. (2018) NGLview-interactive molecular graphics for Jupyter notebooks. *Bioinformatics (Oxford, England)* **34**, 1241–1242
88. Workman, C. T., Yin, Y., Corcoran, D. L., Ideker, T., Stormo, G. D., and Benos, P. V. (2005) enoLOGOS: a versatile web tool for energy normalized sequence logos. *Nucl. Acids Res.* **33**, W389–W392
89. Sievers, F., Wilm, A., Dineen, D., Gibson, T. J., Karplus, K., Li, W., *et al.* (2011) Fast, scalable generation of high-quality protein multiple sequence alignments using clustal Omega. *Mol. Syst. Biol.* **7**, 539
90. Reimer, L., Zepke, U., Moesch, J., Schulze-Hillert, S., Ross-Messemer, M., *et al.* (1992) *EELSpectroscopy. A Reference Handbook of Standard Data for Identification and Interpretation of Electron Energy Loss Spectra and for Generation of Electron Spectroscopic Images*, Carl Zeiss, Oberkochen, Germany